



1 **Global sea-level budget and ocean-mass budget, with focus on advanced data**
2 **products and uncertainty characterisation**

3
4
5

6 **Authors**

7 Martin Horwath (1), Benjamin D. Gutknecht (1), Anny Cazenave (2,3), Hindumathi Kulaippan
8 Palanisamy (2, 4), Florence Marti (2), Ben Marzeion (5), Frank Paul (6), Raymond Le Bris (6), Anna
9 E. Hogg (7), Inès Otosaka (8), Andrew Shepherd (8), Petra Döll (9,10), Denise Cáceres (9), Hannes
10 Müller Schmied (9, 10), Johnny A. Johannessen (11), Jan Even Øie Nilsen (11,12), Roshin P. Raj (11),
11 René Forsberg (13), Louise Sandberg Sørensen (13), Valentina R. Barletta (13), Sebastian B. Simonsen
12 (13), Per Knudsen (13), Ole Baltazar Andersen (13), Heidi Randall (13), Stine K. Rose (13), Christopher
13 J. Merchant (14), Claire R. Macintosh (14), Karina von Schuckmann (15), Kristin Novotny (2), Andreas
14 Groh (2), Marco Restano (16), Jérôme Benveniste (17).

15

16 (1) Technische Universität Dresden, Institut für Planetare Geodäsie, Dresden, D;

17 (2) LEGOS Toulouse, F;

18 (3) International Space Science Institute, Bern, Switzerland

19 (4) Centre for Climate Research Singapore, Meteorological Service Singapore, Singapore

20 (5) Institut of Geography and MARUM - Center for Marine Environmental Sciences, University of
21 Bremen, Bremen, Germany

22 (6) University of Zurich, CH;

23 (7) University of Leeds, UK;

24 (8) Centre for Polar Observation and Modelling, University of Leeds, UK;

25 (9) Institute of Physical Geography, Goethe University Frankfurt, Frankfurt am Main, D;

26 (10) Senckenberg Leibniz Biodiversity and Climate Research Centre (SBiK-F), Frankfurt am Main, D

27 (11) Nansen Environmental and Remote Sensing Center, Bergen, NO;

28 (12) Institute of Marine Research, Bergen, NO.

29 (13) Technical University of Denmark, DK;

30 (14) University of Reading and National Centre for Earth Observation, UK;

31 (15) Mercator Ocean International, Toulouse, F;

32 (16) Serco/ESRIN, I

33 (17) ESA ESRIN, I

34

35 **Correspondence**

36 Martin Horwath, martin.horwath@tu-dresden.de



37 Abstract

38 Studies of the global sea-level budget (SLB) and the global ocean-mass budget (OMB) are essential to
39 assess the reliability of our knowledge of sea-level change and its contributions. Here we present datasets
40 for times series of the SLB and OMB elements developed in the framework of ESA's Climate Change
41 Initiative. We use these datasets to assess the SLB and the OMB simultaneously, utilising a consistent
42 framework of uncertainty characterisation. The time series, given at monthly sampling, include global
43 mean sea-level (GMSL) anomalies from satellite altimetry; the global mean steric component from Argo
44 drifter data with incorporation of sea surface temperature data; the ocean mass component from Gravity
45 Recovery and Climate Experiment (GRACE) satellite gravimetry; the contribution from global glacier
46 mass changes assessed by a global glacier model; the contribution from Greenland Ice Sheet and
47 Antarctic Ice Sheet mass changes, assessed from satellite radar altimetry and from GRACE; and the
48 contribution from land water storage anomalies assessed by the WaterGAP global hydrological model.
49 Over the period Jan 1993 – Dec 2016 (P1, covered by the satellite altimetry records), the mean rate
50 (linear trend) of GMSL is $3.05 \pm 0.24 \text{ mm yr}^{-1}$. The steric component is $1.15 \pm 0.12 \text{ mm yr}^{-1}$ (38% of
51 the GMSL trend) and the mass component is $1.75 \pm 0.12 \text{ mm yr}^{-1}$ (57%). The mass component includes
52 $0.64 \pm 0.03 \text{ mm yr}^{-1}$ (21% of the GMSL trend) from glaciers outside Greenland and Antarctica, $0.60 \pm$
53 0.04 mm yr^{-1} (20%) from Greenland, $0.19 \pm 0.04 \text{ mm yr}^{-1}$ (6%) from Antarctica, and 0.32 ± 0.10
54 mm yr^{-1} (10%) from changes of land water storage. In the period Jan 2003 – Aug 2016 (P2, covered by
55 GRACE and the Argo drifter system), GMSL rise is higher than in P1 at $3.64 \pm 0.26 \text{ mm yr}^{-1}$. This is
56 due to an increase of the mass contributions (now about $2.22 \pm 0.15 \text{ mm yr}^{-1}$, 61% of the GMSL trend),
57 with the largest increase contributed from Greenland. The SLB of linear trends is closed for P1 and P2,
58 that is, the GMSL trend agrees with the sum of the steric and mass components within their combined
59 uncertainties. The OMB budget, which can be evaluated only for P2, is also closed, that is, the GRACE-
60 based ocean-mass trend agrees with the sum of assessed mass contributions within uncertainties.
61 Combined uncertainties (1-sigma) of the elements involved in the budgets are between 0.26 and
62 0.40 mm yr^{-1} , about 10% of GMSL rise. Interannual variations that overlie the long-term trends are
63 coherently represented by the elements of the SLB and the OMB. Even at the level of monthly anomalies
64 the budgets are closed within uncertainties, while also indicating possible origins of remaining
65 misclosures.



66 1 Introduction

67 Sea level is an important indicator of climate change. It integrates effects of changes of several
68 components of the climate system. About 90% of the excess heat in Earth's current radiation imbalance
69 is absorbed by the global ocean (von Schuckmann et al., 2016, 2020; Oppenheimer et al., 2019). About
70 3% melts ice (Slater et al., 2021), while the remaining heat warms the atmosphere (1-2%) and the land
71 (~5%). Present-day global mean sea-level (GMSL) rise primarily reflects thermal expansion of sea
72 waters (the steric component) and increasing ocean mass due to land ice melt, two processes attributed
73 to anthropogenic global warming (Oppenheimer et al., 2019). Anthropogenic changes in land water
74 storage (LWS) constitute an additional contribution to the change in ocean mass (Wada et al., 2017;
75 Döll et al., 2014), modulated by effects of climate variability and change (Reager et al., 2016; Scanlon
76 et al., 2018).

77 To assess the accuracy and reliability of our knowledge about sea-level change and its causes,
78 assessments of the sea-level budget (SLB) are indispensable. Closure of the sea-level budget implies
79 that the observed changes of GMSL equal the sum of observed (or otherwise assessed) contributions,
80 namely the effect of ocean-mass change (OMC) and the steric component (e.g. WCRP, 2018). Steric
81 sea-level can be further separated into volume changes through ocean salinity (halosteric) and ocean
82 temperature (thermosteric) effects, from which the latter is known to play a dominant role in
83 contemporary GMSL rise. Closure of the ocean mass budget (OMB) implies that the observed OMC
84 (e.g., from the Gravity Recovery and Climate Experiment, GRACE, Tapley et al., 2019) is equal to
85 assessed changes of water mass (in solid, liquid or gaseous state) outside the ocean, which are dominated
86 by mass changes of land ice (glaciers and ice sheets) and water stored on land as liquid water or snow.
87 Misclosure of these budgets indicates errors in the assessment of some of the components (including
88 effects of undersampling) or contributions from unassessed elements in the budget.

89 Over the course of its five assessment reports and its recent Special Report on The Ocean and Cryosphere
90 in a Changing Climate (SROCC; IPCC, 2019), the Intergovernmental Panel on Climate Change (IPCC)
91 has documented a significant improvement in our understanding of the sources and impacts of global
92 sea-level rise. Today, the SLB for the period since 1993 is often considered closed within uncertainties
93 (Church et al., 2013, Oppenheimer et al., 2019). Recent studies that reassessed the SLB over different
94 time spans and using different datasets include the studies by Rietbroek et al. (2016), Chambers et al.
95 (2017), Dieng et al. (2017), Chen et al. (2017, 2020), Nerem et al. (2018), Royston et al. (2020) and
96 Vishwakarma et al. (2020). In the context of the Grand Challenge of the World Climate Research
97 Programme (WCRP) entitled “Regional Sea-level and Coastal Impacts”, an effort involving the sea-
98 level community worldwide assessed the various datasets used to estimate components of the SLB
99 during the altimetry era (1993 to present) (WCRP, 2018). A large number of available quality datasets
100 were used for each component, from which ensemble means for each component were derived for the
101 budget assessment.

102 Significant challenges remain. The IPCC SROCC reported the sum of assessed sea-level contributions
103 for the 1993–2015 period (2006–2015 period) to be 2.76 mm yr^{-1} (3.00 mm yr^{-1} , respectively), and this
104 was 0.40 mm yr^{-1} smaller (0.58 mm yr^{-1} smaller) than the observed GMSL rise at 3.16 mm yr^{-1}



105 (3.58 mm yr⁻¹) (Oppenheimer et al., 2019, Table 4.1). While the misclosure was within the combined
106 uncertainties of the sum of contributions and the observed GMSL, these uncertainties were large, with
107 a 90% confidence interval width of 0.74 mm yr⁻¹ to 1.1 mm yr⁻¹. Determining the LWS contribution to
108 sea-level is a particular challenge (WCRP, 2018): Hydrological models suggest LWS losses and
109 therefore a positive contribution from LWS to GMSL rise, while GRACE analyses suggest LWS gains
110 and therefore a negative GMSL contribution from LWS. Challenges of SLB assessments include the
111 question of consistency among the various involved datasets and their uncertainty characterisations. For
112 example, the study by WCRP (2018) assessed each budget element from a large number of available
113 datasets generated in different frameworks and used ensemble means of these datasets in the budget
114 assessment.

115 ESA's Climate Change Initiative (CCI, <https://climate.esa.int>) offers a consistent framework for the
116 generation of high-quality and continuous space-based records of Essential Climate Variables (ECVs;
117 Bojinski et al., 2014). A number of CCI projects has addressed ECVs relevant for the SLB, most
118 importantly the Sea-level CCI project, the Sea Surface Temperature (SST) CCI project, the Glaciers
119 CCI project, the Greenland Ice Sheet CCI project and the Antarctic Ice Sheet CCI project.

120 The Sea-level Budget Closure CCI (SLBC_cci) project conducted from 2017 to 2019 was the first cross-
121 ECV project within CCI. It assessed and utilised the advanced quality of CCI products for SLB and
122 OMB analyses. For this purpose, the project also developed new data products based on existing CCI
123 products and on other data sources. It is specific to SLBC_cci, and complementary to the WCRP
124 initiative, that SLBC_cci concentrated on datasets generated within CCI or by project members. The
125 thorough insights into the genesis and uncertainty characteristics of the datasets facilitated progress
126 towards working in a consistent framework of product specification, uncertainty characterization, and
127 SLB analysis.

128 In this paper we present the methodological framework of the SLBC_cci budget assessments (Sect. 2).
129 We describe the datasets used, including summaries of the methods of their generation and details on
130 their uncertainty characterisation (Sect. 3). We report and discuss results of our OMB and SLB
131 assessments (Sect. 4 to 7) address the data availability in Sect. 8 and conclude in Sect. 9 with an outlook
132 on suggested work in the sequence of this initial CCI cross-ECV study.

133 The analysis concentrates on two time periods: P1 from Jan 1993 to Dec 2016 (the altimetry era), and
134 P2 from Jan 2003 to Aug 2016 (the GRACE/Argo era). The start of P1 is guided by the availability of
135 altimetry data. Its end is guided by the availability of outputs of the WaterGAP Global Hydrological
136 Model used in this study to compute LWS, due to availability of climate input data at the time of the
137 study. The start of P2 is guided by the availability of quality GRACE gravity field solutions at the time
138 of the study and by the implementation of the Argo drifter array. We note, though, that Argo-based steric
139 assessments are uncertain in the early Argo years 2003–2004. The budgets are assessed for mean rates
140 of change (linear trends) over P1 and P2 as well as for GMSL and ocean mass anomalies at monthly
141 resolution. The OMB assessment also addresses the seasonal cycle.



142 2 Methodological framework

143 2.1 Sea-level budget and ocean-mass budget

144 The SLB (e.g., WCRP, 2018) expresses the time-dependent sea-level change $\Delta SL(t)$ as the sum of its
145 mass component $\Delta SL_{\text{Mass}}(t)$ and its steric component $\Delta SL_{\text{Steric}}(t)$:

$$146 \quad \Delta SL(t) = \Delta SL_{\text{Mass}}(t) + \Delta SL_{\text{Steric}}(t). \quad (1)$$

147 The three budget elements are spatial averages over a fixed ocean domain. We consider the global ocean
148 area in a first instance and we discuss restrictions to sub-areas further below.

149 More specifically, $\Delta SL(t)$ is the geocentric sea-level change from which effects of glacial isostatic
150 adjustment (GIA) were corrected (Tamisea, 2011; WCRP, 2018). Likewise, assessments of $\Delta SL_{\text{Mass}}(t)$
151 include corrections for GIA effects. The small elastic deformations of the ocean bottom (Frederikse et
152 al., 2017, Vishwakarma et al., 2020) are not corrected in $\Delta SL(t)$ in this study (cf. Section 3.8). The steric
153 component $\Delta SL_{\text{Steric}}(t)$ arises from the temporal variations of the height of the sea-water columns of a
154 given mass per unit area in response to temporal variations of the temperature and salinity profiles. The
155 mass component $\Delta SL_{\text{Mass}}(t)$ is defined as

$$156 \quad \Delta SL_{\text{Mass}} = \frac{1}{A_{\text{Ocean}} \rho_W} \Delta M_{\text{Ocean}} \quad (2)$$

157 where ΔM_{Ocean} is the change of ocean mass within the ocean domain, A_{Ocean} is the surface area of this
158 domain (defined as $361 \cdot 10^6 \text{ km}^2$), and $\rho_W = 1000 \text{ kg m}^{-3}$ is the density of water. Change of A_{Ocean} is
159 considered negligible over the assessment period. Equivalently, the mass component can be expressed
160 by a spatial average of the geographically dependent change of ocean mass per surface area, $\Delta \kappa_{\text{Ocean}}(x,t)$
161 (with units of kg m^{-2}):

$$162 \quad \Delta SL_{\text{Mass}} = \frac{1}{\rho_W} \langle \Delta \kappa_{\text{source}} \rangle_{\text{Ocean}} \quad (3)$$

163 where $\langle \cdot \rangle_{\text{Ocean}}$ denotes the spatial averaging over the ocean domain.

164 The OMB equation reads

$$165 \quad \Delta M_{\text{Ocean}} = -(\Delta M_{\text{Glaciers}} + \Delta M_{\text{Greenland}} + \Delta M_{\text{Antarctica}} + \Delta M_{\text{LWS}} + \text{other}), \quad (4)$$

166 where $\Delta M_{\text{Glaciers}}(t)$, $\Delta M_{\text{Greenland}}(t)$, $\Delta M_{\text{Antarctica}}(t)$ and $\Delta M_{\text{LWS}}(t)$ are the temporal changes in mass of
167 glaciers outside Greenland and Antarctica (where ice caps are also referred to as glaciers), the Greenland
168 Ice Sheet (GrIS) and Greenland peripheral glaciers, the Antarctic Ice Sheet (AIS), and LWS,
169 respectively. Other terms (e.g., atmospheric water content variations) were not considered in this
170 assessment. We express the OMB in terms of sea-level change,

$$171 \quad \Delta SL_{\text{Mass}} = \Delta SL_{\text{Glaciers}} + \Delta SL_{\text{Greenland}} + \Delta SL_{\text{Antarctica}} + \Delta SL_{\text{LWS}} + \Delta SL_{\text{other}} \quad (5)$$

172 by setting

$$173 \quad \Delta SL_{\text{Source}} = -\frac{1}{A_{\text{Ocean}} \rho_W} \Delta M_{\text{Source}}, \quad (6)$$

174 where the suffix "source" stands for Glaciers, Greenland, Antarctica, or LWS.



175 By expressing the mass component as the sum of the individual mass contributions, the SLB can be
176 expressed as

$$177 \quad \Delta SL = (\Delta SL_{\text{Glaciers}} + \Delta SL_{\text{Greenland}} + \Delta SL_{\text{Antarctica}} + \Delta SL_{\text{LWS}} + \Delta SL_{\text{other}}) + \Delta SL_{\text{Steric}}. \quad (7)$$

178 For each of the budget equations (1), (5) and (7), we refer to the individual terms on both sides of the
179 equation as budget elements. We define the budget misclosure as the difference 'left-hand side minus
180 right-hand side'.

181 Part of this study refers to the SLB over the ocean area between 65°N and 65°S. This choice is made
182 because both altimetry and the Argo system have reduced coverage and data quality in the polar oceans.
183 When referring to a non-global ocean domain, the concept of spatial averaging implied in ΔSL , $\Delta SL_{\text{Steric}}$
184 and ΔSL_{Mass} still holds. However, in this case, the evaluation of ΔSL_{Mass} by the sum of contributions
185 from continental mass sources (Eq. 5 and 6) needs assumptions on the proportions that end up in the
186 specific ocean domain (e.g., Tamisiea et al., 2011), that is, on the geographical distribution of water
187 mass change per surface area, $\Delta \kappa_{\text{source}}$, induced by these continental sources. Based on such assumptions,
188 $\Delta SL_{\text{source}}$ may be evaluated as

$$189 \quad \Delta SL_{\text{source}} = \frac{1}{\rho_W} \langle \Delta \kappa_{\text{source}} \rangle_{\text{Ocean}}. \quad (8)$$

190 Here we assume $\langle \Delta \kappa_{\text{source}} \rangle_{\text{Ocean}} = \langle \Delta \kappa_{\text{source}} \rangle_{\text{GlobalOcean}}$, where the suffix "GlobalOcean" refers to
191 the global ocean, as opposed to a more general ocean domain "Ocean". Our assumption is a
192 simplification of reality. For example, the gravitationally consistent redistribution of ocean water
193 induces geographically dependent sea-level fingerprints (Tamisiea et al., 2011).

194 2.2 Time series analysis

195 The budget assessment is based on anomaly time series $z(t)$ of state parameters, such as sea-level, glacier
196 mass, etc., where $z(t)$ is the *difference* between the state at epoch t and a reference state Z_0 . In SLBC_cci,
197 the reference state Z_0 is defined as the mean state over the ten years from Jan 2006 to 2015. This choice
198 (as opposed to alternative choices such as the state at the start time of the time series) affects plots of
199 $z(t)$ by a simple shift along the ordinate axis. However, uncertainties of $z(t)$ depend more substantially
200 on the choice of Z_0 , which is why they cannot be characterised and analysed without an explicit
201 definition of the reference state. The epoch t usually denotes a time interval such as a calendar month,
202 so that $z(t)$ is a mean value over this period.

203 An alternative way of representing temporal changes is by the rates of change $\frac{\Delta z}{\Delta t}(t)$, where t refers to a
204 time interval with length Δt (e.g. a month or a year) and Δz is the change of z during that interval.
205 Cumulation of $\frac{\Delta z}{\Delta t}(t)$ over discrete time steps gives $z(t)$:

$$206 \quad z(t) = \sum_{\tau=t_0}^t \frac{\Delta z}{\Delta t}(\tau) \Delta t. \quad (9)$$

207 We chose to primarily use the representation $z(t)$ rather than $\frac{\Delta z}{\Delta t}(t)$, that is, we use the evolution of state
208 rather than its rate of change. The choice is motivated by the characteristics of data products from



209 satellite altimetry, satellite gravimetry, and Argo floats. They mostly use the representation $z(t)$. Their
210 differentiation with respect to time amplifies the noise inherent to the observation data.

211 We analyse the budgets on different temporal scales: First, we analyse the linear trends that arise from
212 a least squares regression according to

$$213 \quad z(t) = a_1 + a_2 t + a_3 \cos(\omega_1 t) + a_4 \sin(\omega_1 t) + a_5 \cos(2\omega_1 t) + a_6 \sin(2\omega_1 t) + \varepsilon(t), \quad (10)$$

214 where a_1 is the constant part, a_2 is referred to as the linear trend, or simply the trend, and $\omega_1 = 2\pi \text{ yr}^{-1}$.
215 The parameters a_3, \dots, a_6 are co-estimated when considering time series that temporally resolve a
216 seasonal signal that has not been removed beforehand. We use the trend a_2 as a descriptive statistic to
217 quantify the mean rate of change in a way that is well-defined and robust against noise. The trend a_2
218 thus obtained for different budget elements is then evaluated in budget assessments according to Eq. (1),
219 (5) and (7).

220 We apply an unweighted regression in Eq. (10). While a weighted regression may better account for
221 uncertainties, it would imply that episodes of true interannual variation get different weights in the time
222 series of different budget elements, so that the trends a_2 would be less comparable across budget
223 elements. As an exception, we apply a weighted regression in one case (the SLBC_cci steric product,
224 Sect. 3.2.2) where otherwise biases in the early years of the time series would bias the trend.

225 Second, we analyse the budget on a time series level, that is, we evaluate the budget equations (1), (5)
226 and (7) for $z(t)$ per epoch. For this purpose, the time series need to be interpolated to an identical monthly
227 temporal sampling, while for the regression analysis they are left at their specific temporal sampling.

228 2.3 Uncertainty characterisation

229 Following the ‘Guide to the expression of uncertainty in measurement’ (JCGM, 2008) we quantify
230 uncertainties of a measurement (including its corrections) in terms of the second moments of a
231 probability distribution that “characterises the dispersion of the values that could reasonably be
232 attributed to the measurand”. Specifically, we use the standard uncertainty (i.e. standard deviation, 1-
233 sigma) to characterise the uncertainty of a measured value. See Merchant et al. (2017) for a recent review
234 on uncertainty information in the CCI context.

235 Uncertainty propagation is applied when manipulating and combining different measured values.
236 Correlation of errors, where present, significantly affects the uncertainty in combined quantities and
237 careful treatment is required in the context of a budget study in which many millions of measured values
238 are combined. In this study we have utilised and significantly advanced the characterisation of temporal
239 error correlations and their accounting in uncertainty propagations, such as for the uncertainty of linear
240 trends. Where no error correlations are present, the uncertainty of a sum (or difference) of values is the
241 root sum square of the uncertainties of the individual values. Uncorrelated uncertainty propagation is
242 applied, in particular, for assessing uncertainties of the sum (or difference) of budget elements since the
243 data sources for these contributions are mostly independent.

244 Within this framework for uncertainty characterisation, the uncertainty assessment of each budget
245 element used a methodology appropriate to the data. Their description in Sect. 3 documents the variety



246 of approaches, including different ways how error correlations are accounted for explicitly or implicitly.
247 The requirement to refer $z(t)$ consistently to the mean over the 2006–2015 reference period entailed
248 adaptations of the uncertainty characterisation for some of the elements.

249 For each budget element, uncertainties of the linear trends were assessed by the project partners who
250 contribute the datasets on the budget element. By accounting for temporal error correlations, the trend
251 uncertainties are typically larger than the formal uncertainty that would arise from the least squares
252 regression (Eq. 10). Our concept of treating the trend purely as a mathematical functional of the full
253 time series through which uncertainties can be propagated implies that our evaluated uncertainties in
254 trends arise only from uncertainties in $z(t)$ and not from statistical fitting effects, such as any true
255 nonlinear evolution of $z(t)$ or sampling any assumed underlying trend from a short series of data.

256 3 Data sets

257 3.1 Global mean sea-level

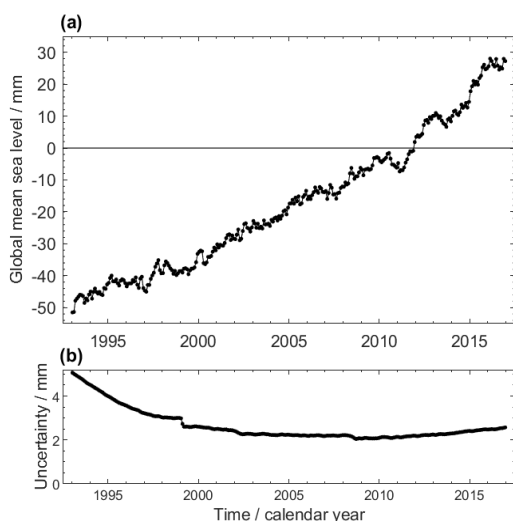
258 *Methods and product*

259 We use time series of Global Mean Sea-Level (GMSL) anomalies derived from satellite altimetry
260 observations. For the period Jan 1993 – Dec 2015, the GMSL record is the version 2.0 of the ESA
261 (European Space Agency) CCI (Climate Change Initiative) ‘Sea-level’ project ([http://www.esa-](http://www.esa-sealevel-cci.org/)
262 [sealevel-cci.org/](http://www.esa-sealevel-cci.org/)). The CCI sea-level record combines data from the TOPEX/Poseidon, Jason-1/2,
263 GFO, ERS-1/2, Envisat, CryoSat-2 and SARAL/Altika missions and is based on a new processing
264 system (Ablain et al., 2015, 2017a; Quartly et al., 2017; Legeais et al., 2018). It is available as a global
265 gridded $1^\circ \times 1^\circ$ resolution dataset over the 82°N – 82°S latitude range. It has been validated using
266 different approaches including a comparison with tide gauge records as well as to ocean re-analyses and
267 climate model outputs. The GMSL record is extended with the Copernicus Marine Environment and
268 Monitoring Service dataset (CMEMS, <https://marine.copernicus.eu/>) from Jan 2016 to Dec 2016.

269 The TOPEX-A instrumental drift due to aging of the TOPEX-A altimeter placed in the TOPEX/Poseidon
270 mission from Jan 1993 to early 1999 was corrected for in the GMSL time series following the approach
271 of Ablain et al. (2017b). It was derived by comparing TOPEX-A sea-level data with tide gauge data. The
272 TOPEX-A drift value based on this approach amounts to $1.0 \pm 1.0 \text{ mm yr}^{-1}$ over Jan 1993 to Jul 1995
273 and to $3 \pm 1.0 \text{ mm yr}^{-1}$ over Aug 1995 to Feb 1999 (see also WCRP, 2018).

274 For the SLBC_cci project, the gridded sea-level anomalies were averaged over the 65°N – 65°S latitude
275 range. The GMSL time series was corrected for GIA applying a value of -0.3 mm yr^{-1} (Peltier, 2004).
276 Annual and semi-annual signals were removed through a least square fit of 12-months and 6-months
277 period sinusoids.

278 Figure 1a shows the record of GMSL anomalies. The well-known, sustained GMSL rise has a linear
279 trend of $3.05 \pm 0.24 \text{ mm yr}^{-1}$ over P1. An overall increase of the rate of sea-level rise over the 24 years
280 is visible (cf. Nerem et al., 2018). The overall GMSL rise is superimposed by interannual variations like
281 the temporary GMSL drop between 2010 and 2011 by about 6 mm (cf. Boening et al., 2012) with a
282 subsequent return to the rising path.



283

284

285

286

Figure 1: (a) Global (65°N to 65°S) mean sea-level time series at its monthly resolution. Changes are expressed with respect to the mean of the reference interval 2006–2015. (b) The assessed standard uncertainties.

287 *Uncertainty assessment*

288 Over the recent years, several articles (Ablain et al., 2015, 2017b; Dieng et al, 2017; Quartly et al., 2017;
289 Legeais et al., 2018) have discussed sources of errors in GMSL trend estimation. Ablain et al. (2019)
290 extended these previous studies by considering new altimeter missions (Jason-2, Jason-3) and recent
291 findings on altimetry error estimates. We use the uncertainty assessment by Ablain et al. (2019), which
292 can be summarised as follows:

293 Three major types of errors are considered in the GMSL uncertainty: (a) biases between successive
294 altimetry missions characterised by bias uncertainties at any given time; (b) drifts in GMSL due to on-
295 board instrumental drifts or long-term drifts such as the error in the GIA correction, orbit etc.
296 characterised by a linear trend uncertainty, and (c) other measurement errors such as geophysical
297 correction errors (wet tropospheric, orbit, etc.) which exhibit temporal correlations and are characterised
298 by their standard deviation. These error sources are assumed to be independent from each other.

299 For each error source, the variance-covariance matrix over all months is calculated from a large number
300 of random trials (>1000) of simulated errors with a standard normal distribution. The total error
301 variance-covariance matrix is the sum of the individual variance-covariance matrices of each error
302 source. The GMSL uncertainties per epoch are estimated from the square root of the diagonal terms of
303 the total matrix. The covariances are rigorously propagated to assess the uncertainties of multi-year
304 linear trends. In the present study we use standard uncertainties, while Ablain et al. (2019) quote 1.65-
305 sigma uncertainties. Ablain et al. (2019) refer to GMSL anomalies with respect to the mean over a 1993–
306 2017 reference period, while our study uses the 2006–2015 reference period. We neglect the effect of
307 this difference on the uncertainties.



308 Fig. 1b shows the GMSL anomaly uncertainties per epoch. They are larger during the TOPEX/Poseidon
309 period (3 mm to 6 mm) than during the Jason period (close to 2.5 mm). This is mainly due to
310 uncertainties of the TOPEX-A drift correction. Long-term drift errors common to all missions also
311 increase the uncertainties towards the interval boundaries.

312 3.2 Steric sea-level

313 3.2.1 Ensemble mean steric product for 1993–2016

314 Since the Argo-based steric product developed within SLBC_cci (see Section 3.2.2 below) does not
315 cover the full P1 period, for P1 we resort to the existing ensemble mean steric product by Dieng et al.
316 (2017), updated to include the year 2016. It comprises the following three datasets for the period 1993–
317 2004: the updated versions of Ishii and Kimoto (2009), NOAA dataset (Levitus et al., 2012) and EN4
318 dataset (Good et al., 2013). Over the recent years, these datasets integrate Argo data from IPRC
319 (International Pacific Research Center,
320 http://apdrc.soest.hawaii.edu/projects/Argo/data/gridded/On_standard_levels/), JAMSTEC (Japan
321 Agency for Marine-Earth Science and Technology,
322 ftp://ftp2.jamstec.go.jp/pub/argo/MOAA_GPV/Glb_PRS/OI/) and SCRIPPS (SCRIPPS Institution of
323 Oceanography (http://sioargo.ucsd.edu/RG_Climatology.html). Annual and semi-annual signals were
324 removed. The uncertainty was characterised from the spread between the ensemble members and, where
325 available, from uncertainties given for the individual ensemble members.

326 Figure 2 shows the ensemble mean steric time series. It exhibits an overall rise, modulated by
327 interannual fluctuations which are within uncertainties prior to 2005 but exceed assessed uncertainties
328 later, e.g. in 2010/2011.

329 3.2.2 SLBC_cci Steric product

330 Within SLBC_cci, the calculation scheme for the steric sea-level change based on Argo data was
331 updated from that described by von Schuckmann and Le Traon (2011). Formal propagation of
332 uncertainty was included following JCGM (2008, their Eq. 13) in which an overall uncertainty estimate
333 is obtained by propagating and combining the evaluations of uncertainty associated with each source.

334 *Methods and product*

335 The steric thickness anomaly for a layer, l , of water with density ρ_l is $h'_l = h_l - h_{l,c}$, where $h_{l,c}$ is the
336 steric thickness of a layer with climatological temperature and salinity and $h_l = \left(\frac{1}{\rho_l} - \frac{1}{\rho_0}\right) \rho_0 \Delta z_{l0}$ is the
337 “steric thickness” of the layer *relative to a layer of reference density* ρ_0 and reference height Δz_0 . h'_l can
338 therefore be written in terms of layer density ρ_l and climatological density for the layer $\rho_{l,c}$ as

$$339 \quad h'_l = \left(\frac{1}{\rho_l} - \frac{1}{\rho_{l,c}}\right) \rho_0 \Delta z_{l0}. \quad (11)$$

340 The monthly mean steric thickness anomaly for layer, l , is found as the optimum combination of the
341 steric thickness anomaly calculations from all the valid profiles in the grid cell for the month. Let the



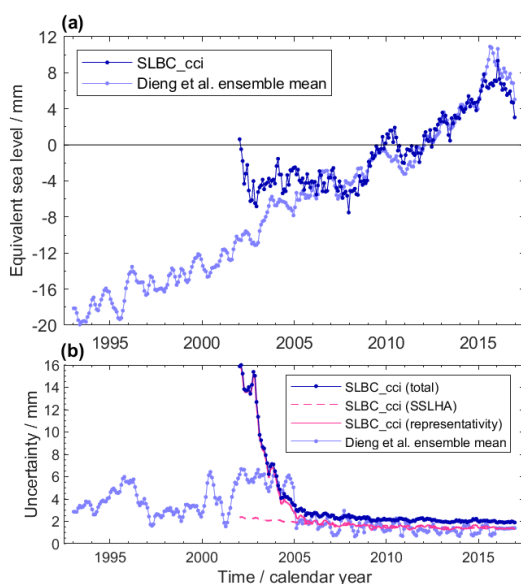
342 individual anomaly calculations be collected in a vector \mathbf{x}_l . The optimum estimate is then given by the
 343 following collection of equations:

$$344 \quad \mathbf{h}'_l = \mathbf{w}_l^T \mathbf{x}_l \quad (12)$$

$$345 \quad \mathbf{w}_l = \frac{1}{\mathbf{1}^T \mathbf{S}_{x_l}^{-1} \mathbf{1}} \mathbf{S}_{x_l}^{-1} \mathbf{1}, \quad (13)$$

346 where $\mathbf{1}$ is a column vector of 1s, \mathbf{w}_l is the vector of weights appropriate to a minimum error variance
 347 average, and \mathbf{S}_{x_l} is the error covariance matrix of the steric thickness anomaly estimates.

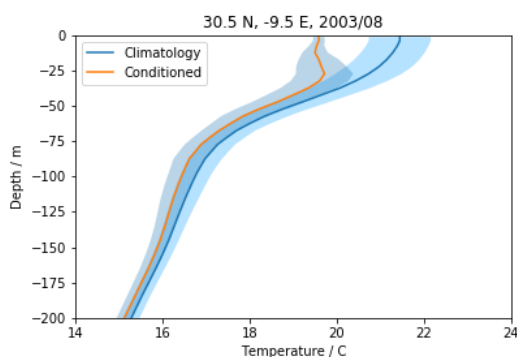
348 The error covariance matrix, \mathbf{S}_{x_l} , is needed for the optimal calculation of the monthly average in Eq.
 349 (12), as well as for the evaluation of uncertainty discussed below. To estimate this matrix, we need to
 350 be clear about what “error” means here: it is the difference between the steric thickness anomaly for the
 351 layer from a single profile (Argo, or climatological) and the (unknown) true cell-month mean. This
 352 difference therefore has two components: the measurement error in the profile, characterised by an error
 353 covariance \mathbf{S}_{x_m} ; and a representativeness error arising from variability within the cell-month \mathbf{S}_{x_r} . The
 354 measurement error covariance is the smaller term and was modelled to be independent between profiles
 355 within the cell (neglecting the fact that on occasion a single Argo float will contribute more than one
 356 profile within a given cell in a month). The representativeness error covariance was modelled assuming
 357 that this error has an exponential correlation form with a length scale of 2.5° and time scale of 10 days.



358
 359 **Figure 2:** (a) Global (65°N to 65°S) mean steric sea-level height anomaly time series at monthly resolution.
 360 Dark blue: dataset generated within SLBC_cci based on Argo data and the CCI SST product. Light blue:
 361 Update of the ensemble mean product by Dieng et al. (2017). Changes are expressed with respect to the
 362 mean of the reference interval 2006-2015. (b) uncertainties assessed for the estimates in (a). Pink curves
 363 (dashed and full lined) show the uncertainty contribution from the SSLHA uncertainty and from the global
 364 representativity uncertainty, respectively.



365 It is relatively common for there to be layers with no observations, sometimes in the upper ocean and
366 often at depth. Conditional climatological profiles were used as an additional “observation” to fill in
367 information for missing-data layers. The climatology of profiles was conditioned by the observed SST
368 from Merchant et al. (2019), which essentially has negligible sampling uncertainty at monthly cell-
369 average scales. The SST information constrains the upper-ocean profile to a degree determined by the
370 vertical correlation of variability, which is variable in time and place according to the mixed layer depth.
371 The uncertainty in the conditional climatological profile is the variability. Examples of an unconditional
372 and conditional climatological profile are shown in Fig. 3. For this particular month (August), year
373 (2003) and location (30.5°N, -9.5°E), the SST is about 2°C below the climatological value. The
374 conditioning is strong for the upper ~50 m of the ocean, and within this modest depth range the
375 conditioned profile is realistic given the SST (approximately isothermal over a mixed layer). The
376 uncertainty is reduced at the surface, where the cell-month SST is well known from the satellite data.
377 Below about 150 m, the effect of conditioning decays towards zero (conditioned and unconditioned
378 profiles converge).



379

380 **Figure 3:** Example of effect of conditioning climatology using SST from SST_cci, for a single time and
381 location (30.5°N, -9.5°E, August 2003). Unconditioned (blue) and conditioned (orange) temperature
382 profiles with their uncertainty ranges (blue-shaded).

383 Including SST information slightly reduces uncertainty and affects steric height in the mixed layer often
384 enough to influence the global mean. Over the period 2005–2018 the trend in steric height is larger using
385 SST-conditioned climatological profiles than when using a static climatology as the prior. The use of
386 static climatology to fill gaps in Argo profiles has been shown to cause systematic underestimates of
387 trends in the literature (e.g., Ishii and Kimoto, 2009). Inclusion of SST-conditioning to the climatology
388 mitigates the over-stabilising effect.

389 Steric sea level height anomalies (SSLHA) were calculated for every month from Jan 2002 to Dec 2017
390 in a global grid of 5° × 5° spatial resolution. For a given cell-month the SSLHA is the sum of the layer-
391 by-layer estimates of steric thickness anomaly, i.e., $h' = \sum_l h'_l$. By concatenating the vectors \mathbf{w}_l^T and \mathbf{x}_l
392 for all the layers into a vector of weights \mathbf{w} and a vector of thicknesses \mathbf{x} we can write the equivalent
393 equation

394
$$\mathbf{h}' = \mathbf{w}^T \mathbf{x}. \tag{14}$$



395 This form makes it more clear how to estimate the uncertainty in the SSLHA, which is

$$396 \quad u_{h'} = (\mathbf{w}^T \mathbf{S}_x \mathbf{w})^{0.5}. \quad (15)$$

397 To evaluate the uncertainty we need to formulate \mathbf{S}_x . The diagonal blocks corresponding to each layer
398 in \mathbf{S}_x are the matrices \mathbf{S}_{x_l} that have already been calculated on a layer-by-layer basis. Assumptions about
399 the error correlations between layers are then required in order to complete the off-block-diagonal
400 elements of \mathbf{S}_x . Conservative assumptions were made:

- 401 • Measurement errors are perfectly correlated vertically in a given profile; this is equivalent to
402 saying that the sensor calibration bias dominates all other sources of measurement uncertainty
403 in each profile.
- 404 • Representativity errors are perfectly correlated vertically.

405 Having obtained cell-month mean SSLHA estimates and associated uncertainty, the global mean steric
406 sea-level height anomaly, $\Delta SL_{\text{Steric}}$, is the area-weighted average of the available gridded SSLHA results.
407 $\Delta SL_{\text{Steric}}$ was calculated over the range 65°S to 65°N, consistent with other budget elements.

408 Figure 2a shows the $\Delta SL_{\text{Steric}}$ time series from the SLBC_cci product. While from 2005 onwards, the
409 trends of the SLBC_cci product and the ensemble mean product (cf. Table A1) as well as their
410 interannual behaviour are similar, the SLBC_cci product shows little change prior to 2005. This
411 difference and its reflection by the uncertainty characterization are discussed further below.

412 *Uncertainty assessment*

413 The uncertainties of the available cell-month mean SSLHA estimates were propagated to the $\Delta SL_{\text{Steric}}$.
414 In any given month, there are missing SSLHA cells, through lack of sufficient Argo profiles. Using
415 $\Delta SL_{\text{Steric}}$ estimated from the available SSLHA cells as an estimate for the global steric sea-level anomaly
416 introduces a global representativity uncertainty. Moreover, the global sampling errors are correlated
417 from month-to-month because the sampling distribution evolves over the course of several years towards
418 near-global representation. To evaluate the global representativity uncertainty and serial correlation, the
419 sampling pattern of sparse years was imposed on near-complete fields: the standard deviation of the
420 difference in global mean with the two sampling patterns is a measure of uncertainty. The correlation
421 between the sample-driven difference in consecutive months was found to be 0.85. The time series of
422 the global representativity uncertainty, the uncertainty propagated from the gridded SSLHA uncertainty
423 (which has no serial correlation) and this correlation coefficient combine to define a full error covariance
424 estimate to be obtained for the $\Delta SL_{\text{Steric}}$ time series.

425 Figure 2b shows the two components of uncertainty (global representativity and propagated SSLHA
426 uncertainty) together with the total uncertainty. The global representativity uncertainty dominates prior
427 to 2005 and is very large in 2002 and 2003. This reflects how sparse and unrepresentative the sampling
428 by the Argo network was at that early stage.

429 Given the large representativity uncertainty prior to 2005, the absence of an increase in the SLBC_cci
430 steric record during that time is thus understood to arise from global sampling error and is consistent
431 with the global sampling uncertainty. The SLBC_cci steric time series and the ensemble mean steric
432 time series are consistent given the evaluated uncertainties throughout the record. In addition, the



433 evaluated uncertainties for the two time series with their different ways of uncertainty assessment are
434 remarkably similar for the period of the established Argo network starting from 2005, giving confidence
435 in the validity of two very distinct approaches to uncertainty characterisation.

436 The use of a formal uncertainty framework allows separation of distinct uncertainty issues, namely, our
437 ability to parameterise and estimate the various uncertainty terms, our ability to estimate the error
438 covariance, and the model for propagation of error at each successive step.

439 Two aspects of the uncertainty model are recognised to be potentially optimistic: the modelling of
440 measurement errors as independent between profiles rather than platforms; and the use of only 10 years
441 for assessing inter-annual variability. Two assumptions are potentially conservative: measurement errors
442 in salinity and temperature were combined in their worst-case combination; representativity errors in
443 profiles are assumed to be fully correlated vertically, whereas in reality they are likely to decorrelate
444 over large vertical separations.

445 A significant output of the uncertainty modelling of the steric component is the error covariance matrix
446 for the time series. It enables proper quantification of the change during the time series. We employed
447 the time-variable uncertainties to determine the linear trend in a weighted regression according to Eq.
448 (10). Without weighting, the global sampling error prior to around 2005, noted above, would bias any
449 fitted trend result. Use of the error covariance matrix enables proper quantification of the uncertainty in
450 the trend calculation by propagating the error covariance matrix through the trend function. Without
451 this, the serial correlation in the global sampling error would be neglected, and the calculated trend
452 uncertainty would be an underestimate.

453 3.2.3 Deep ocean steric contribution

454 For the deep ocean below 2000 m depth, the steric contribution was assessed as a linear trend of
455 $0.1 \pm 0.1 \text{ mm yr}^{-1}$ based on Purkey and Johnson (2010). This deep ocean contribution is included in the
456 ensemble mean steric product described in Sect. 3.2.2. This deep-ocean component is added to the Argo-
457 based SLBC_cci steric product described in Sect. 3.2.1 (which is for depths <2000 m) in order to address
458 the full ocean steric contribution.

459 3.3 Ocean-mass change

460 *Methods and product*

461 Time series of ocean-mass change (OMC), in terms of anomalies with respect to the 2006-2015 reference
462 period, were generated from monthly gravity field solutions of the GRACE mission (Tapley et al., 2019).
463 Similar to previous analyses (Johnson and Chambers 2013, Uebbing et al., 2019) we used spherical
464 harmonic (SH) GRACE solutions in order to have full control on the methodology and uncertainty
465 assessment. Greater detail is provided by Horwath et al. (2019).

466 The following GRACE monthly gravity field solutions series were considered:



- 467 • ITSG-Grace2018 (Mayer-Gürr et al., 2018a, 2018b) from Institut für Geodäsie, Technische
468 Universität Graz, Austria, with maximum SH degree 60 (data source
469 ftp://ftp.tugraz.at/outgoing/ITSG/GRACE/ITSG-Grace2018/monthly/monthly_n60)
470 • CSR_RL06 from Center for Space Research at University of Texas, Austin, TX, USA,
471 GFZ_RL06 from Helmholtz Centre Potsdam GFZ German Research Centre for Geosciences,
472 Germany, JPL_RL06 from Jet Propulsion Laboratory, Pasadena, California, USA, all with
473 maximum SH degree 60 (data source: <https://podaac.jpl.nasa.gov/GRACE>).

474 We chose ITSG-Grace2018 as the preferred input SH solution because it showed the lowest noise level
475 among all releases considered, with no indication for differences in the contained signal (Groh et al.,
476 2019b).

477 Gravity field changes were converted to equivalent water height (EWH) surface mass changes according
478 to Wahr et al. (1998). The total mass anomaly over an area like the global ocean was derived by spatial
479 integration of the EWH changes. We used the unfiltered GRACE solutions in order to avoid damping
480 effects from filtering. A 300 km wide buffer zone along the ocean margins was excluded from the spatial
481 integration. Around islands, the buffer was applied if their surface area exceeds a threshold, which was
482 set to 20,000 km² in general and 2,000 km² for near-polar latitudes beyond 50°N or 50°S. The integral
483 was subsequently scaled by the ratio between total area of the ocean domain and the buffered integration
484 area. Effects due to the uneven global ocean-mass redistribution are part of the leakage uncertainty
485 assessment.

486 Modelled short-term atmospheric and oceanic mass variations are accounted for within the gravity field
487 estimation procedure (Flechtner et al., 2014; Dobslaw et al., 2013) and are not included in the monthly
488 solutions. To retain the full mass variation effect, the monthly averages of the modelled atmospheric and
489 oceanic dealiasing fields were added back to the monthly solutions by using the so-called GAD products
490 (Flechtner et al., 2014). We subsequently removed the spatial mean of atmospheric surface pressure over
491 the full ocean domain. Our investigations confirmed findings by Uebbing et al. (2019) on the
492 methodological sensitivity of this procedure. If the GAD averages were calculated over only the buffered
493 area, OMC trends would be about 0.3 mm yr⁻¹ higher than for our preferred approach.

494 In order to include the degree-one components of global mass redistribution (not determined by
495 GRACE) we implemented the approach by Swenson et al. (2008) further developed by Bergmann-Wolf
496 et al. (2014) which combines the GRACE solutions for degree $n \geq 2$ with assumptions on the ocean-mass
497 redistribution. We also replaced GRACE-based C_{20} components by results from satellite laser ranging
498 (Cheng et al., 2013, https://podaac-tools.jpl.nasa.gov/drive/files/allData/grace/docs/TN-11_C20_SLR.txt).

499 GIA implies redistributions of solid Earth masses and (to a small extent) of ocean masses. We corrected
500 the gravity field effect of GIA-related mass redistributions by using three different GIA modelling
501 results: The model by A et al. (2013), based on ICE-5Gv2 glaciation history from Peltier (2004); the
502 model ICE-6G_C (VM5A) by Peltier et al. (2015); and the mean solution by Caron et al. (2018). The
503 correction was applied on the level of the SH representation. Our preferred GIA correction is the one by
504 Caron et al. (2018). It is based on the ICE-6G deglaciation history (Peltier et al., 2015), while the model
505 by A et al. (2013) is based on its predecessor model ICE-5G. Furthermore, while the models by A et al.
506 (2013) and Peltier et al. (2015) are single GIA models, the solution by Caron et al. (2018) arises as a



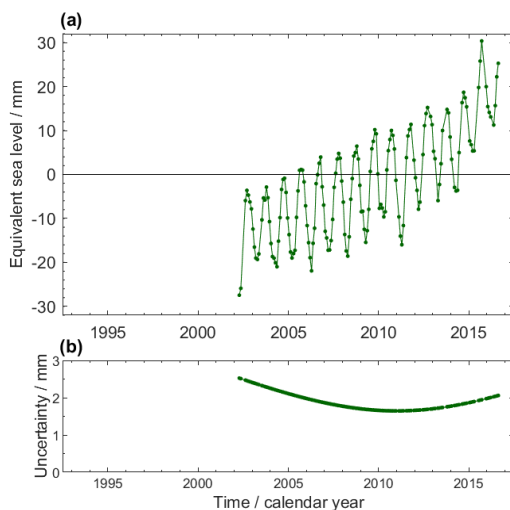
507 weighted mean from a large ensemble of models, where the glaciation history and the solid Earth
 508 rheology have been varied and tested against independent geodetic data to provide probabilistic
 509 information. Table 1 demonstrates the sensitivity of GRACE OMC solutions to the GIA correction.

510 **Table 1:** OMC linear trends [mm equivalent global mean sea-level per year] over Jan 2003 – Aug 2016
 511 from different GRACE solutions. Each column uses a different GIA correction as indicated in the header
 512 line. The first four lines of data show results from different SH solution series generated within SLBC_cci.
 513 Numbers in brackets are for the ocean domain between 65°N and 65°S. The last two lines show external
 514 products, namely the ensemble mean of the updated time series by Johnson and Chambers (2013) and the
 515 GSFC v2.4 mascon solution. The last column shows the assessed total uncertainty of the trend. The
 516 preferred solution is printed in bold font. The GSFC mascon trend is over the period Jan 2003 – Jul 2016.

	GIA from Caron et al. (2018)	GIA from Peltier et al. (2015)	GIA from A et al. (2013)	Uncertainty
ITSG-Grace2018	2.19 (2.18)	1.93 (1.87)	1.99 (1.89)	0.22 (0.25)
CSR RL06 sh60	2.17 (2.16)	1.91 (1.86)	1.97 (1.87)	0.22 (0.25)
GFZ RL06 sh60	2.10 (2.12)	1.84 (1.81)	1.90 (1.83)	0.22 (0.25)
JPL RL06 sh60	2.19 (2.19)	1.93 (1.88)	1.99 (1.90)	0.22 (0.25)
Chambers ensemble	n/a	n/a	2.17	n/a
GSFC v2.4 mascons	n/a	n/a	2.25 (2.12)	n/a

517

518 Figure 4a shows our preferred time series of the mass contribution to sea level (see Fig. 10 for a time
 519 series where the seasonal signal is subtracted). The overall trend at $2.19 \pm 0.22 \text{ mm yr}^{-1}$ over P2 is
 520 superimposed by a seasonal signal with 10.3 mm amplitude of annual sinusoid and by interannual
 521 variations like a drop by about 6 mm sea level equivalent between 2010 and 2011.



522

523 **Figure 4:** (a) Ocean-mass component of GMSL change, derived from the ITSG-Grace2018 spherical
 524 harmonic GRACE monthly solutions with a GIA correction according to Caron et al. (2018). Mass change
 525 of the global ocean is expressed in terms of equivalent GMSL change with respect to the mean of the
 526 reference interval 2006–2015. Time series are shown in their original temporal sampling where some
 527 months are missing. (b) Uncertainties assessed for the estimates in (a).



528 Overall, integrated OMC time series were generated from four series of SH GRACE solutions, using
529 three GIA corrections (and the option of no GIA correction), for the global ocean and the ocean domain
530 between 65°N and 65°S. For comparison, we also considered OMC time series from two external
531 sources: Global OMC time series from CSR, GFZ and JPL SH solutions by Johnson and Chambers
532 (2013), updated by D. Chambers on 6 November 2017 and made available from
533 https://dl.dropboxusercontent.com/u/31563267/ocean_mass_orig.txt (accessed 26 Jan 2018); Goddard
534 Space Flight Center (GSFC) Mascon solutions v02.4 (Luthcke et al., 2013), dedicated for ocean mass
535 research (data source: <https://earth.gsfc.nasa.gov/geo/data/grace-mascons>). Time series of total OMC
536 were derived by the weighted integral over all oceanic points using the ocean-land point-set mask
537 provided with the GSFC Mascon solutions. We strictly used the area information provided with the
538 GSFC dataset and rescaled the resulting mass change to the standard ocean surface area of $361 \cdot 10^6$ km²
539 used within SLBC_cci.

540 *Uncertainty assessment*

541 The following sources of uncertainty are relevant (cf. Nagler et al., 2018b):

- 542 • GRACE errors: Errors in the GRACE observations as well as in the modelling assumptions
543 applied during GRACE processing propagate into the GRACE products.
- 544 • Errors in C_{20} and degree-one terms: Errors in these components, due to their very large scale
545 nature and possible systematic effects are particularly important for global OMC applications
546 (cf. Quinn and Ponte, 2010; Blazquez et al., 2018; Loomis et al., 2019).
- 547 • The impact of GIA on GRACE gravity field solutions is a significant source of signal and error
548 for mass change estimates. Current models show strong discrepancies (Quinn and Ponte, 2010;
549 Chambers et al., 2010; Tamisiea, 2011; Rietbroek et al., 2016; Blazquez et al., 2018).
- 550 • Leakage errors arise from the vanishing sensitivity of GRACE to small spatial scales (high SH
551 degrees). In SLBC_cci, GRACE data were used up to a degree 60 (~333 km half-wavelength).
552 As a result, signal from the continents (e.g. ice-mass loss) leaks into the ocean domain.
553 Differences in methods to avoid (or repair) leakage effects can amount to several tenths of
554 kg m⁻² yr⁻¹ in regional OMC estimates (e.g., Kusche et al., 2016). Our buffering approach does
555 not fully avoid leakage. Moreover, the upscaling of the integrated mass changes to the full ocean
556 area is based on the assumption that the mean EWH change in the buffer is equal to the mean
557 EWH change in the buffered ocean integration kernel.

558 We adapted the uncertainty assessment approach used for GRACE-based products of the Antarctic Ice
559 Sheet CCI project (Nagler et al., 2018b). We modelled errors as the combination of two components
560 distinguished by their temporal characteristics: temporally uncorrelated noise, with variance σ_{noise}^2
561 assumed equal for each month; and systematic errors of the linear trend, with an associated uncertainty
562 σ_{trend} . This model is a simplification as it does not consider autocorrelated errors other than errors that
563 evolve linearly with time. The uncertainty $\sigma_{\text{total}}(t)$ per epoch t in a time series of mass anomalies $z(t)$
564 is approximated as

$$565 \quad \sigma_{\text{total}}^2(t) = \sigma_{\text{noise}}^2 + \sigma_{\text{trend}}^2 (t - t_0)^2, \quad (16)$$



566 where t_0 is the centre of the reference interval to which $z(t)$ refers.
567 The noise was assessed from the GRACE OMC time series themselves as detailed by Groh et al. (2019a).
568 The de-trended and de-seasonalised time series were high-pass filtered in the temporal domain. The
569 variance of the filtered time series was assumed to be dominated by noise. This variance was scaled by
570 a factor that accounts for the dampening of uncorrelated noise variance imposed by the high-pass
571 filtering. The assessed noise component comprises uncorrelated errors from all uncertainty sources
572 except for GIA, which is considered purely linear in time.
573 The systematic errors of the linear trends are assumed to originate from errors in degree-one
574 components, C_{20} , the GIA correction, and from leakage. The related uncertainties were assessed for each
575 source individually and summed in quadrature. For example, the GIA uncertainty assessment was based
576 on the small sample of GIA correction options. The standard deviation over the sample of the three GIA
577 model options was taken as the standard uncertainty of the GIA correction. The same approach was
578 applied for the degree-one uncertainty and for the C_{20} uncertainty. To estimate the uncertainty that arises
579 from leakage, in conjunction with buffering and rescaling, we performed a simulation study based on
580 synthetic mass change data from the ESA Earth System Model (ESM; Dobslaw et al., 2015). The ESM
581 data were processed according to the settings of the SLBC_cci OMC analysis and the results (simulated
582 observations) were compared with the OMC that arises from the full-resolution ESM data (simulated
583 truth). In order to derive statistics for multi-year trends, we calculated linear trends of the simulated
584 observations and of the simulated truth and of their misfit for every interval of a length between 9 years
585 and 12 years contained in the ESA-ESM period. The weighted RMS of misfits over all intervals was
586 taken as the estimate of the leakage error uncertainty.
587 Results of the uncertainty assessment for the ITSG-Grace2018-based OMC solutions are summarised in
588 Table 2. Figure 4b shows the time-dependent uncertainties associated to the ocean mass contribution
589 time series. They reflect their construction by Eq. (16), where away from 2011.0, the uncertainty of the
590 linear trend contributes an increasing share.

591 **Table 2:** Assessed uncertainty components for the OMC solutions based on the ITSG-Grace2018 SH
592 GRACE solutions.

Uncertainty component	global ocean domain	ocean domain 65°S – 65°N
Temporally uncorrelated noise	1.65 mm	1.77 mm
Trend uncertainty degree-one	0.14 mm yr ⁻¹	0.14 mm yr ⁻¹
Trend uncertainty C_{20}	0.05 mm yr ⁻¹	0.07 mm yr ⁻¹
Trend uncertainty GIA	0.14 mm yr ⁻¹	0.17 mm yr ⁻¹
Trend uncertainty leakage	0.10 mm yr ⁻¹	0.09 mm yr ⁻¹
Trend uncertainty combined	0.22 mm yr ⁻¹	0.25 mm yr ⁻¹

593



594 3.4 Glacier contribution

595 *Methods and product*

596 The glacier mass change estimate was derived by updating the global glacier model (GGM) of Marzeion
597 et al. (2012). Annually reported direct mass balance observations (using the glaciological method) are
598 available for only a few hundred of the roughly 215.000 existing glaciers (Zemp et al., 2019). Global-
599 scale geodetic, altimetric and gravimetric observations are limited to the most recent decades (e.g.,
600 Bamber et al., 2018). Only at a regional scale and more disperse, geodetic glacier mass changes are
601 available back into the 1960s (e.g. Maurer et al., 2019; Zhou et al., 2018). The overall objective of the
602 model approach is to use observations of glacier mass change for calibration and validation of the glacier
603 model, which then translates information about atmospheric conditions into glacier mass change, taking
604 into account various feedbacks between glacier mass balance and glacier geometry. This enables a
605 reconstruction of glacier change that is complete in time and space, and that has higher temporal
606 resolution than the observations (here, we use monthly output). In our analysis, we included all glaciers
607 outside of Greenland and Antarctica, and separately reconstructed the glacier change for Greenland
608 peripheral glaciers.

609 As initial conditions, we used glacier outlines obtained from the Randolph Glacier Inventory (RGI)
610 version 6.0 (updated from Pfeffer et al., 2014). The time stamp of these outlines differs between glaciers,
611 but typically is around the year 2000. To obtain results before this time, the model uses an iterative
612 process to find that glacier geometry in the year of initialisation (e.g., 1901) that results in the observed
613 glacier geometry in the year of the outline's time stamp (e.g., 2000) after the model was run forward.

614 The model relies on monthly temperature and precipitation anomalies to calculate the specific mass
615 balance of each glacier. It uses the gridded climatology of New et al. (2002) as a baseline. Here, we used
616 seven different sources of atmospheric conditions (as well as their mean) as boundary conditions (Harris
617 et al., 2014; Saha et al., 2010; Compo et al., 2011; Dee et al., 2011; Kobayashi et al., 2015; Poli et al.,
618 2016; Gelaro et al., 2017). Temperature is used to estimate the ablation of glaciers following a
619 temperature-index melt model, and to estimate the solid fraction of total precipitation, which is used to
620 estimate accumulation. Glacier area and length change are estimated following mass change based on
621 volume-area-time scaling, allowing for a delayed response of glacier geometry to glacier mass change.
622 A detailed description of the model is provided by Marzeion et al. (2012).

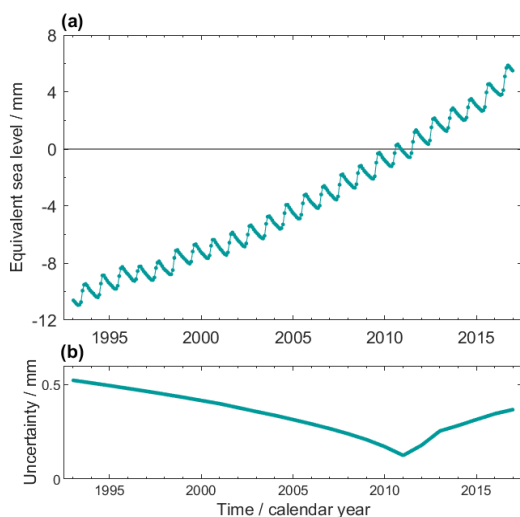
623 There are four global model parameters that need to be optimised: (i) the air temperature above which
624 melt of the ice surface is assumed to occur; (ii) the temperature threshold below which precipitation is
625 assumed to be solid; (iii) a vertical precipitation gradient used to capture local precipitation patterns not
626 resolved in the forcing datasets; and (iv) a precipitation multiplication factor to account for effects from
627 (among other processes) wind-blown snow and avalanching, which are not resolved in the forcing
628 dataset. For each of the eight forcing datasets cited above, we performed a multi-objective optimisation
629 for these four parameters, using a leave-one-glacier-out cross validation to measure the model's
630 performance on glaciers for which no mass balance observations exist. We used annual in-situ
631 observations from about 300 glaciers, covering a total of almost 6000 mass balance years (WGMS,
632 2018). In the optimisation, the temporal correlation of observed and modelled mass balances is



633 maximised, the temporal variance of modelled mass balances is brought close to that of observed mass
634 balances (aiming for a realistic sensitivity of the model to climate variability and change), and the model
635 bias is minimised (to avoid an artificial trend in modelled glacier mass). Using the mean of the seven
636 atmospheric datasets described above results in the overall best model performance. Compared to the
637 results in Marzeion et al. (2012), the correlation of annual glacier mass change was increased from 0.60
638 to 0.64, the bias was changed from 5 kg m^{-2} to -4 kg m^{-2} (both statistically indistinguishable from zero),
639 and the ratio of the temporal variance of modelled and observed mass balances was improved from 0.83
640 to 1.00.

641 The model output for each glacier is aggregated on a regular 0.5° by 0.5° grid, where the mass change
642 of each glacier is assigned to the grid cell that contains the glacier's centre point, even if the glacier
643 might cover several grid cells (the GGM does not calculate the spatial distribution of mass changes of a
644 glacier, so that a more accurate spatial assignment to the grid is not possible). Regional or global values
645 of glacier mass change were obtained by summing over the region of interest.

646 Figure 5a shows the global glacier contribution to GMSL anomalies (see Fig. 10 and 12 for time series
647 after subtraction of the seasonal signal). The glacier contribution has a linear trend of 0.64 ± 0.03
648 mm yr^{-1} over P1, where the positive rate increases from the first half to the second half of the period.
649 Interannual variations are less pronounced than for other budget elements.



650

651 **Figure 5:** (a) Global glacier mass contribution to GMSL assessed by the GGM at a monthly resolution.
652 Peripheral glaciers in Greenland and Antarctica are not included. Glacier mass change is expressed in terms
653 of equivalent GMSL change with respect to the mean of the reference interval 2006–2015. (b)
654 uncertainties assessed for the estimates in (a).

655 *Uncertainty assessment*

656 The root mean square error obtained during the cross validation was propagated through the model.
657 Since the evaluation of the model results does not indicate any temporal or spatial correlation of the



658 model errors, the uncertainty of temporal and spatial mass change aggregations was calculated assuming
659 independence of the model errors, i.e. by taking the root of the summed squares of each glacier's (and
660 year's) uncertainty.

661 Uncertainties of mass anomalies with respect to the mean over the 2006–2015 interval were
662 approximated by uncertainties of anomalies with respect to the centre of the interval, 2011.0.
663 Uncertainties of yearly mass change rates were aggregated (as root sum square) forward or backward
664 from 2011.0 to the specific epochs. Figure 5c show the uncertainties per epoch, reflecting this
665 aggregation from 2011.0. Uncertainties of multi-year linear trends were calculated as follows: The
666 uncertainties of yearly rates of mass change were aggregated in time over the interval of interest, leading
667 to an uncertainty of cumulated mass change over the interval of interest, which was subsequently divided
668 by the length of the interval. That is, the trend uncertainty was calculated as the root sum square of
669 yearly rate uncertainties, divided by the interval length.

670 3.5 Greenland contribution

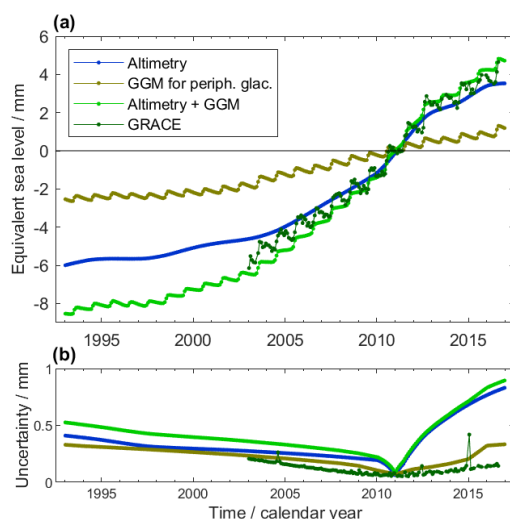
671 Changes of land ice masses in Greenland comprising the GrIS and peripheral glaciers are assessed in
672 two ways: by GRACE (Sect. 3.5.1) and by a combination of satellite altimetry for the GrIS and glacier
673 modelling for the peripheral glaciers (Sect. 3.5.2, 3.5.3). Results from those complementary assessments
674 shown in Fig. 6 are collectively discussed at the end of this section.

675 3.5.1 GRACE-based estimates

676 The GRACE-based product developed at DTU Space within the Greenland Ice Sheet CCI project is used
677 to provide mass change estimates for the GrIS from GRACE monthly gravity field solutions. The quasi-
678 monthly GRACE-based mass anomaly estimates (grids and basin time series) are available from
679 <https://climate.esa.int/en/projects/ice-sheets-greenland/>. Comprehensive descriptions and references
680 are given by Barletta et al. (2013), Sørensen et al. (2017), Horwath et al. (2019) and Mottram et al.
681 (2019).

682 *Methods and product*

683 An inversion technique was used to obtain monthly mass anomalies for entire Greenland from each of
684 the available GRACE monthly solutions, with the approach described in Barletta et al. (2013). An
685 icosahedral grid of point masses, each representing an area of ~20 km radius, was inverted in order to
686 fit the gravity observations at the satellite altitude. The limited ~300 km resolution of GRACE monthly
687 solution requires inversion for ice mass changes over the whole GrIS including peripheral glaciers,
688 whose contribution cannot be isolated independently. For this work the CSR RL06 monthly solutions
689 was used, with a maximum degree and order of 96, and prior to the inversion the prescribed C₂₀ and
690 degree-one corrections were applied, together with an anisotropic filtering (DDK3 from Kusche et al.,
691 2009). Mass changes of glaciers outside Greenland were co-estimated to minimise their leakage into the
692 Greenland ice mass change estimates.



693

694 **Figure 6:** (a) Greenland ice mass contribution to GMSL assessed from GRACE (dark green) and from the
695 combination of altimetry and GGM (light green). The altimetry-based assessment for the ice sheet (blue)
696 and the GGM-based assessment for the peripheral glaciers (brown) are also shown. Ice mass change is
697 expressed in terms of equivalent GMSL change with respect to the mean of the reference interval 2006–
698 2015. GRACE-based time series are shown in their original temporal sampling where some months are
699 missing. (b) uncertainties assessed for the estimates in (a).

700 Our inversion did not include a GIA correction. We separately calculated the effect of GIA on our
701 inversion. Based on the Caron et al. (2018) GIA solution (chosen for consistency with the OMC
702 estimate, cf, Sect. 3.3) we obtained a GIA effect of 7.5 Gt yr^{-1} . This linear trend was subtracted from the
703 time series.

704 *Uncertainty assessment*

705 GRACE based products are provided with error estimates based on the approach developed by Barletta
706 et al. (2013). The uncertainties were propagated from the errors in GRACE monthly solutions, leakage
707 errors due to GRACE limited spatial resolutions, and errors in the models used to account for degree-
708 one contributions and the GIA correction. In detail, the uncertainty related to GRACE solutions was
709 obtained in a Monte-Carlo-like approach, with 200 simulations for Stokes coefficients selected from a
710 zero-mean normal distribution, and the standard deviation from the GRACE CSR RL06 Level 2
711 solution.

712 *3.5.2 Altimetry-based estimates*

713 *Methods and product*

714 The surface elevation changes estimates are based on satellite radar altimeter observations for the period
715 1992–2017, and include data from the missions ERS-1, ERS-2, Envisat and Cryosat-2. The temporal
716 evolution of surface elevation is estimated by a combination of cross-over, repeat-track and least-square



717 methods covering the entire GrIS and for the entire time span covered by the different missions, on a 5
718 km common uniform grid (Sørensen et al., 2018). The different characteristics of the missions (the
719 conventional radar altimetry of the ERS-1, ERS-2 and Envisat missions, and the novel SAR
720 Interferometric altimetry of Cryosat-2), and the different orbital characteristics call for special care in
721 the combinations of the different datasets, and in the determination of the uncertainties.

722 Before an ice sheet wide estimate of volume change can be converted into ice sheet mass balance,
723 contributions which are not related to ice-mass change must be corrected for. These contributions
724 include factors such as changes in firn compaction rates, GIA, and elastic uplift. Such a correction
725 method was first applied for satellite ICESat lidar observation (Sørensen et al., 2011). As Ku-band radar
726 altimetry is subject to weather-induced changes in subsurface penetration depth of snow-covered areas
727 (Nilsson et al., 2015), we here chose to apply a different calibration procedure instead of the direct
728 correction fields. The calibration period is the era of ICESat (2003–2009), where the ICESat laser
729 altimeter provides precise estimates of surface elevation change without surface penetration, and
730 ENVISAT provides similar estimates subject to surface penetration. The spatial differences between the
731 ICESat and ENVISAT mass estimates provides the input for a calibration field (initial radar-volume
732 mass balance, Simonsen et al., 2021, which can be applied to the full time series of elevation changes
733 based on satellite radar altimeter observations for the period 1992–2017. This approach follows that of
734 Simonsen et al., 2021.

735 Following the calibration procedure described above, we computed monthly grids of mass change rates
736 at $100 \times 100 \text{ km}^2$ resolution for the entire main GrIS. The peripheral glaciers were excluded from the
737 grid. For each epoch, the mass rates of the grid cells were added to derive monthly mass change rates of
738 the entire ice sheet. Time series of ice sheet mass anomalies with respect to the reference interval 2006–
739 2015 were then generated by cumulating the mass change rates in time and subtracting the mean over
740 2006–2015 from the cumulated time series.

741 The monthly grids were derived by applying a temporal window to aggregate the radar observations.
742 For the ERS-1, ERS-2, and ENVISAT mission, this window is 5 years long. For CryoSat-2 the
743 window is 3 years long. The monthly grids are referred to the centre of the time window. This result in
744 a smoothening of the time series to resolve climatic changes and not seasonal weather.

745 *Uncertainty assessment*

746 The error of the traditional altimetry-based mass-change estimates originates from different sources:
747 uncertainty in the interpolation from point changes to ice sheet wide changes, uncertainty in the bedrock
748 movement and in the firn compaction model, uncertainties due to the neglect of basal melt contributions,
749 and of the possible ice accumulation above the Equilibrium Line Altitude due to ice dynamics. For
750 observations from radar altimetry, an additional source of uncertainty is the changing radar penetration
751 in the firn column. The latter was circumvented by the calibration approach applied here.

752 The overall uncertainty in the altimetry-derived mass change time series is provided as a conservative
753 estimate based on converting the radar altimetry volume error into mass by ascribing ice densities to all
754 grid cells. This estimate is assumed to be slightly overestimating the combined error of the five error
755 sources.



756 Uncertainties of cumulated mass changes (in space as well as in time) were derived as follows: For the
757 cumulation in space, standard uncertainties from all grid cells were added linearly. For the cumulation
758 in time, uncertainties of mass change rates were aggregated (as root sum square) forward or backward
759 from 2011.0 to the specific epochs. Uncertainties of multi-year trends were calculated as the aggregated
760 uncertainties of mass change rates over the interval of interest, divided by the interval length.

761 3.5.3 Altimetry-GGM combination

762 Unlike the GRACE-based assessment for Greenland, the altimetry-based assessment does not include
763 Greenland peripheral glaciers. We therefore take the sum of the altimetry-based estimates for the ice
764 sheet and GGM-based estimates for the peripheral glaciers to represent the total ice mass changes in
765 Greenland. The GGM methods and products and the related uncertainty assessments described in Sect.
766 3.4 were applied. The uncertainties of the sum of the two products were calculated as the root sum square
767 of the uncertainties of the two summands.

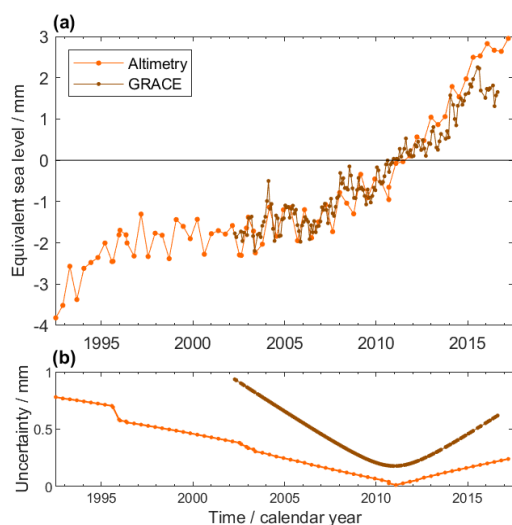
768 The synthesis of assessed Greenland GMSL contributions in Fig. 6a shows that both the proper ice sheet
769 and peripheral glaciers contribute significantly ($0.43 \pm 0.04 \text{ mm yr}^{-1}$ and $0.17 \pm 0.02 \text{ mm yr}^{-1}$,
770 respectively, over P1). The rates of change vary interannually, peaking in 2011 and 2012. This is
771 consistently reflected in the GRACE-based estimate and in the altimetry-GGM combination. The
772 altimetry-GGM combination shows a somewhat larger trend over P2 than the GRACE-based estimate
773 ($0.89 \pm 0.07 \text{ mm yr}^{-1}$ versus $0.78 \pm 0.02 \text{ mm yr}^{-1}$) and does not resolve the annual cycle in the same way
774 as GRACE, as the annual cycle is not resolved in the altimetry-based time series. The time-variable
775 uncertainties of the altimetry-based and GGM-based time series (Fig. 6b) reflect the cumulation of
776 uncertainties of rates of change backward and forward from the reference interval centre. The
777 uncertainties of the GRACE-based time series reflect the superposition of a linear trend uncertainty and
778 an individual uncertainty for each monthly GRACE solution.

779 3.6 Antarctic contribution

780 Mass changes of the AIS are assessed in two ways: by GRACE (Sect. 3.6.1) and by satellite radar
781 altimetry (Sect. 3.6.2). The results from the complementary assessments shown in Fig. 7 are collectively
782 discussed at the end of this section. The contribution from Antarctic peripheral glaciers is discussed in
783 Sect. 3.8.

784 3.6.1 GRACE-based estimates

785 The GRACE-based product developed at TU Dresden within the Antarctic Ice Sheet CCI project is used
786 to provide mass change estimates for the AIS from GRACE monthly gravity field solutions (Horwath
787 and Groh, 2016; Nagler et al., 2018a, 2018b). Quasi-monthly GRACE-based mass anomaly estimates
788 (grids and basin time series) are available from <https://climate.esa.int/en/projects/ice-sheets-antarctica/> or https://data1.geo.tu-dresden.de/ais_gmb.
789



790

791 **Figure 7:** (a) Antarctic Ice Sheet mass change contributions to GMSL from GRACE (dark orange) and
792 altimetry (orange). Ice mass change is expressed in terms of equivalent GMSL change with respect to the
793 mean of the reference interval 2006–2015. The temporal sampling is quasi-monthly (with a few months
794 missing) for the gravimetric time series and 140-daily (with a few shorter time increments) for the altimetric
795 time series. (b) Uncertainties assessed for the estimates in (a).

796 *Methods and product*

797 The Antarctic Ice Sheet GRACE-based products were derived from the SH monthly solution series by
798 ITSG-Grace2016 by TU Graz (Klinger et al., 2016; Mayer-Gürr et al., 2016) following a regional
799 integration approach with tailored integration kernels that account for both the GRACE error structure
800 and the information on different signal variance levels on the ice sheet and on the ocean (Horwath and
801 Groh, 2016). GIA was corrected according to the regional GIA model by Ivins et al. (2013)

802 *Uncertainty assessment*

803 The uncertainty assessment (Nagler et al., 2018b) is analogous to that described for the GRACE OMC
804 assessment in Sect. 3.3. For the AIS, the dominant source of uncertainty is the GIA correction.
805 Uncertainties in the degree-one components and the C_{20} component of the gravity field are also
806 important.

807 *3.6.2 Altimetry-based estimates*

808 *Methods and Data Product*

809 We computed Antarctica mass change from 1992 to 2017 using observations from four different satellite
810 radar altimetry missions – ERS-1, ERS-2, ENVISAT and CryoSat-2 – following the methodology
811 described by Shepherd et al. (2019). For each mission, we computed elevation change from repeated
812 elevation measurements during fixed epochs of 140 days on a polar stereographic grid using a plane fit
813 method (McMillan et al., 2016). We applied a backscatter correction to remove the short-term



814 fluctuations in elevation change correlated with changes in backscatter and we combined the time series
815 from different missions together by applying a cross-calibration technique. To convert our elevation
816 change time series into a mass change time series, we first identified areas of ice dynamical imbalance
817 in order to discriminate between changes occurring at the density of snow and ice. We defined these
818 regions as areas with persistent elevation change that is significantly different from firm thickness change
819 estimates derived from a semi-empirical firm densification model (Ligtenberg et al., 2011). Areas of
820 accelerated rate of ice thickness change were allowed to evolve through time. Based on this empirical
821 classification, we converted our elevation change time series to a mass change time series by using a
822 density of 917 kg m^{-3} in areas classified as ice and using spatially-varying snow densities from the firm
823 densification model in areas classified as snow. The mass anomalies for the WAIS, the EAIS and the
824 APIS at a 140-day resolution from 1992 to 2016 are available from <http://www.cpom.ucl.ac.uk/csopr/>.

825 *Uncertainty assessment*

826 We assessed the uncertainties of our elevation change time series and convert them to a mass change
827 uncertainty using the same time-evolving mask of ice dynamical imbalance areas described in the
828 previous section. At each epoch, we estimated the overall error of our elevation change as the sum in
829 quadrature of systematic errors, time-varying errors, errors associated to the calibration between the
830 different satellite missions and errors associated with snowfall variability. The systematic errors refer to
831 errors that affect the long-term elevation change trend. These may arise from short-term changes in the
832 snowpack properties or from short-lived accumulation events that may not be accounted for in our plane
833 fit model. We quantified the systematic errors as the standard error of the long-term rate of elevation
834 change. The time-varying error refers to errors in the satellite measurements that might hinder our ability
835 to measure elevation change at one particular epoch due to the measurement's precision or non-uniform
836 sampling. We calculated these errors as the average standard error of elevation measurements. The inter-
837 satellite biases uncertainties were computed as the standard deviations between modelled elevations
838 during a two-year period centred on each mission overlap. Finally, we quantified the snowfall variability
839 uncertainty based on estimates from a regional climate model.

840 Cumulated mass changes and their uncertainties were originally generated with respect to the reference
841 epoch 1993.0, separately for the East Antarctic Ice Sheet (EAIS), the West Antarctic Ice Sheet (WAIS),
842 and the Antarctic Peninsula (APIS). To refer the product to the reference interval 2006–2015, we
843 subtracted the respective mean from the mass anomaly time series. We calculated unaccumulated
844 uncertainties by taking the differences between the uncertainties of consecutive epochs. We re-
845 cumulated these uncertainties with respect to the centre of the reference interval, 2011.0, by linearly
846 cumulating the unaccumulated uncertainties, forward or backward, from 2011.0. Uncertainties of linear
847 trends were calculated by linearly cumulating the unaccumulated uncertainties over the interval of interest
848 and division by the interval length. Uncertainties for the mass changes of the entire AIS were calculated
849 as the root sum square of uncertainties for EAIS, WAIS and APIS.

850 Figure 7a shows the AIS GMSL contributions from both the GRACE-based and the altimetry-based
851 assessment. Over P1 (assessed from altimetry), the AIS contribution to GMSL is $0.19 \pm 0.04 \text{ mm yr}^{-1}$.
852 Rates of change are much smaller from 1995 to 2006 and larger from 2006 onwards. Mass losses are
853 dominated by mass losses in West Antarctica due to changing ice flow dynamics (cf. Shepherd et al.,
854 2018). Over P2, the evolution of the AIS GMSL contribution from altimetry and GRACE is similar,



855 with linear trends at $0.34 \pm 0.04 \text{ mm yr}^{-1}$ and $0.27 \pm 0.11 \text{ mm yr}^{-1}$, respectively, overlaid by noise as
856 well as common interannual signal. Time-dependent uncertainties shown in Figure 7b reflect the
857 cumulation with respect to the reference interval centre in the case of the altimetry-based anomalies, and
858 the model analogous to Eq. (16) for the GRACE-based estimates.

859 3.7 Land water storage

860 *Methods and product*

861 The LWS contribution is assessed with the global hydrological model (GHM) WaterGAP (Döll et al.,
862 2003; Müller Schmied et al., 2014) in its latest version, WaterGAP2.2d (Müller Schmied et al., 2021).
863 The model simulates daily water flows and water storage anomalies including the effects of human water
864 use on a $0.5^\circ \times 0.5^\circ$ grid (55 km by 55 km at equator and $\sim 3000 \text{ km}^2$ grid cell) covering the whole land
865 area except for Antarctica (we excluded model outputs over Greenland to avoid double-counting). Note
866 that the Caspian Sea is not comprised in the model grid (based on the WATCH-CRU land-sea mask)
867 and thus not included in the assessment of the LWS component. Water flows are routed through a series
868 of individual water storage compartments (Fig. 2 in Müller Schmied et al., 2021). Following the stream
869 network defined by the global drainage direction map DDM30 (Döll and Lehner 2002), streamflow is
870 laterally routed until reaching the ocean or an inland sink. The model is calibrated against observed
871 mean annual streamflow at 1319 gauging stations (Müller Schmied et al., 2021). LWS anomalies
872 (LWSA) are the aggregation of the anomalies in all individual water storage compartments:

$$873 \quad LWSA = SnWSA + CnWSA + SMWSA + GWSA + LaWSA + ReWSA + WeWSA + RiWSA \quad (17)$$

874 where WSA are water storage anomalies in snow (Sn), canopy (Cn), soil moisture (SM), groundwater
875 (G), lake (La), reservoir (Re), wetland (We) and river (Ri) storages. The model does not account for
876 anomalies related to glacier mass variations. Land areas that in reality are covered by glaciers are
877 represented as non-glacier-covered land areas where hydrological processes (evapotranspiration, runoff
878 generation, groundwater recharge etc.) are simulated. In terms of OMB assessment, adding the glacier
879 contribution (Sect. 3.4) and the LWS contribution has the implication of “double-counting” the land
880 areas covered by glaciers, which are then included in both contributions. In a recent study (Cáceres et
881 al., 2020), time series of glacier mass variations computed by the GGM of Marzeion et al. (2012) were
882 integrated as an input to WaterGAP; this resulted in a non-standard version of the model that explicitly
883 accounts for glaciers. The aggregated water storage anomalies computed by this model version were
884 compared to the result of adding LWSA computed by the standard WaterGAP and anomalies related to
885 glacier mass variations computed by the GGM. The comparison of these two approaches showed that
886 the impact of double-counting glacier-covered areas is insignificant at global scale.

887 Human water use is accounted for through the representation of the impact of water impoundment in
888 man-made reservoirs and of net water abstractions (i.e. total abstractions minus return flows) on water
889 flows and storages. The reservoir operation algorithm implemented in WaterGAP is a slightly modified
890 version of the generic algorithm of Hanasaki et al. (2006) (Döll et al., 2009). Based on a preliminary
891 version of the Global Reservoir and Dam (GRanD) data base (Lehner et al., 2011), the model accounts
892 for the largest 1082 reservoirs. The reservoir filling phase is simulated based on the first operational
893 year and the storage capacity. Net water abstractions are simulated for five water use sectors (irrigation,



894 livestock farming, domestic use, manufacturing industries and cooling of thermal power plants) and
895 subsequently subtracted from the surface water and groundwater storage compartments (Müller
896 Schmied et al., 2021; Döll et al., 2014).

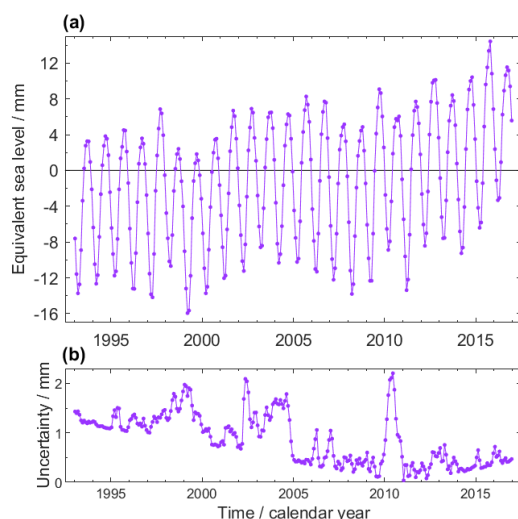
897 In the framework of this study, we used monthly globally-averaged (over 64432 0.5° by 0.5° grid cells)
898 LWSA time series extending from Jan 1992 to Dec 2016. Anomalies are relative to the mean over the
899 period Jan 2006 to Dec 2015. The model was forced with daily WATCH Forcing Data methodology
900 applied to ERA-Interim data (WFDEI, Weedon et al., 2014). Two different variants of this climate
901 forcing were used. In one of them, precipitation was bias corrected using monthly precipitation sums
902 from the Global Precipitation Climatology Centre (GPCC, Schneider et al., 2015) and, in the other one,
903 it was bias corrected using monthly precipitation sums from the Climate Research Unit (CRU, Harris et
904 al., 2014); hereafter, we refer to these climate forcings as WFDEI-GPCC and WFDEI-CRU,
905 respectively. In addition, we considered two different assumptions in relation to consumptive irrigation
906 water use in groundwater depletion regions. Typically, consumptive irrigation water use is calculated
907 by assuming that crops receive enough water for actual evapotranspiration to be equivalent to the
908 potential evapotranspiration value (Döll et al., 2016). We assumed consumptive irrigation water use to
909 be either optimal (i.e. 100% of water requirement) or 70% of optimal in groundwater depletion areas
910 (for more details, see Döll et al., 2014). Consequently, an ensemble of four LWSA time series
911 corresponding to two climate forcings and two irrigation water use variants was considered. The
912 unweighted mean of the four ensemble members was used in the SLB assessment.

913 A comparison of the monthly time series of total water and ice storage anomaly (CMC) over the
914 continents (except Greenland and Antarctica) as derived from GRACE and from the non-standard
915 WaterGAP version with glacier integration showed a very good fit, with a modelling efficiency of 0.87
916 (Cáceres et al., 2020). The GRACE trend during 2003–2016, however, was 26% weaker than the trend
917 from the non-standard WaterGAP version. More recently this difference was significantly reduced after
918 the GRACE analysis for continental total water storage was made more consistent with the GRACE
919 OMC analysis (Gutknecht et al., 2020).

920 Figure 8a shows the monthly time series of LWSA contribution to GMSL. It is characterised by the
921 highest seasonal amplitude of all ocean-mass contributions due to seasonal climate variations. (See Fig.
922 12 for a time series where the seasonal signal is subtracted.) The overall positive trend (0.40 ± 0.10
923 mm yr^{-1} over P1) is caused mainly by groundwater and surface water depletion that more than balances
924 increased land water storage due to the filling of new reservoirs.

925 *Uncertainty assessment*

926 Uncertainties are characterised by the spread between the four model runs. For each month, the standard
927 deviation of the values from the four time series was taken as the standard uncertainty. Figure 8b shows
928 these time-variable uncertainties of the LWSA. They reflect month-to-month differences in the spread
929 between the ensemble members. Since the LWSA anomalies are referred to the 2006–2015 mean value
930 and the four ensemble members show different trend, the uncertainty is lowest around 2011.0 and tends
931 to increase towards the beginning (1993) and the end (2016). The standard deviation of the linear trends
932 calculated for each ensemble member was taken as the standard uncertainty of the linear trend of the
933 ensemble mean.



934

935 **Figure 8:** (a) Contributions from global land water storage changes (except for Greenland and Antarctica)
936 to GMSL, assessed by the WaterGAP global hydrology model at its monthly resolution. Water mass change
937 is expressed in terms of equivalent GMSL change with respect to the mean of the reference interval 2006–
938 2015. (b) uncertainties assessed for the estimates in (a)

939 3.8 Other contributions and issues

940 Caspian Sea water storage changes are not included in the WaterGAP model domain and are therefore
941 not included in our GMSL budget assessment. WCRP (2018) quote this contribution as
942 $0.075 \pm 0.002 \text{ mm yr}^{-1}$ since 1995 and $0.109 \pm 0.004 \text{ mm yr}^{-1}$ since 2002. Based on GRACE analyses,
943 Cáceres et al. (2020) estimate the contribution to be $0.066 \pm 0.003 \text{ mm yr}^{-1}$ over 2003–2016, very
944 similar to the GRACE-based estimate by Loomis and Luthcke (2017), which corresponds to
945 $0.067 \pm 0.007 \text{ mm yr}^{-1}$ sea-level equivalent over 2003–2014.

946 Antarctic peripheral glaciers are neither included in the altimetry-based assessment of the Antarctic ice
947 mass change nor in the GGM assessment. The GRACE-based estimate for Antarctic ice mass changes
948 was designed to address the ice sheet proper but includes part of the mass changes of peripheral glaciers
949 in result of the low spatial resolution capability of satellite gravimetry. Gardner et al. (2013) estimate
950 the Antarctic peripheral glaciers mass loss over 2003–2009 to a value equivalent to
951 $0.017 \pm 0.028 \text{ mm yr}^{-1}$ GMSL. Zemp et al. (2019) estimate a loss over 2006–2016 at a value equivalent
952 to $0.04 \pm 0.30 \text{ mm yr}^{-1}$ GMSL.

953 Changes in atmospheric water content (mainly tropospheric water vapour) are not included in our
954 assessment. The atmosphere stores around 12,700 Gt of water (Trenberth 2014), or 35 mm sea-level
955 equivalent. Hartmann et al. (2013) report that the rate of change of tropospheric water vapour content is
956 very likely consistent with the Clausius–Clapeyron relation (about 7% increase in water content per
957 Kelvin). This corresponds to an equivalent GMSL effect on the order of -0.03 to -0.05 mm yr^{-1} , which
958 was also obtained by Dieng et al. (2017) from ERA-Interim atmospheric reanalysis results. Interannual



959 variations of atmospheric water content reported by Dieng et al. (2017) are up to the order of 1 mm
960 GMSL equivalent.

961 The elastic deformation of the ocean bottom induced by the present-day global redistribution of water
962 and ice loads is not accounted for in our GMSL estimate from satellite altimetry (cf. Sect. 2.1). Since
963 the deformation is downward on average over the global ocean, this omission leads to an
964 underestimation of relative GMSL rise. Frederikse et al. (2017) estimated the effect for the period 1993–
965 2014 to be 0.13 mm yr^{-1} for the global ocean and 0.17 mm yr^{-1} for the domain bounded by $\pm 66^\circ$ latitude,
966 with higher rates in the second half of the period. Vishwakarma et al. (2020) estimated the effect for
967 2005–2015 to be $0.11 \pm 0.02 \text{ mm yr}^{-1}$ for a global altimetry domain buffered along the coasts.

968 Our conversion from OMC (or ocean-mass contributions) to sea-level change adopts the density of
969 freshwater. In previous studies, either the density of fresh water or the density of sea water has been
970 adopted, where both approaches have their justification (cf. Gregory et al., 2019; Vishwakarma et al.,
971 2020). If we had adopted the sea water density (1028 kg m^{-3}), our assessments of mass contributions
972 would be reduced by 2.7%.

973 **4 Ocean-mass budget**

974 We evaluate the OMB according to Eq. (5). We do the assessment for the P2 period (Jan 2003 –Aug
975 2016, cf. Sect. 2.2). We use the OMC assessment made for the global ocean.

976 **4.1 Linear trend**

977 For the elements of the mass budget, we calculated linear trends over P2. We assessed their uncertainties
978 as explained in Sect. 2.3 and specified for every element in Sect. 3. The results are shown in Table 3.

979 All components exhibit a significant positive trend, i.e., water mass loss on land. Greenland ice masses
980 contribute $0.78 \pm 0.02 \text{ mm yr}^{-1}$ as assessed from GRACE or $0.89 \pm 0.07 \text{ mm yr}^{-1}$ as assessed from radar
981 altimetry for the ice sheet and from the GGM for the peripheral glaciers. The glaciers outside Greenland
982 and Antarctica contribute $0.77 \pm 0.03 \text{ mm yr}^{-1}$, similar to Greenland. The Antarctic Ice Sheet's
983 contribution is $0.27 \pm 0.10 \text{ mm yr}^{-1}$ if assessed from GRACE, and $0.34 \pm 0.04 \text{ mm yr}^{-1}$ if assessed from
984 radar altimetry. The trend in land water storage amounts to $0.40 \pm 0.10 \text{ mm yr}^{-1}$.

985 The sum of components is $2.19 \pm 0.15 \text{ mm yr}^{-1}$ and $2.40 \pm 0.13 \text{ mm yr}^{-1}$, respectively, if the Greenland
986 and Antarctica contributions are assessed using either GRACE or altimetry. The corresponding trend in
987 mean global ocean mass according to our preferred GRACE-based solution (ITSG-Grace2018, GIA
988 correction according to Caron et al., 2018) amounts to $2.19 \pm 0.22 \text{ mm yr}^{-1}$.

990 The misclosures of Eq. (5) with combined standard uncertainties are $-0.04 \pm 0.27 \text{ mm yr}^{-1}$ (if using
991 GRACE for Greenland and Antarctica) and $-0.21 \pm 0.26 \text{ mm yr}^{-1}$ (if using altimetry in Greenland and
992 Antarctica). Hence, the mass budget in terms of linear trends is closed within the assessed uncertainties.
993 In view of the systematic uncertainties inherent to several components of the mass budget, we stress that
994 any closure that is much better than the combined uncertainties does not indicate that the components



995 are correct at the level of the budget closure, but may just be a coincidence of trend errors compensating
 996 each other.

997 **Table 3:** Linear trends of the mass budget elements [mm equivalent global mean sea-level per year] for the
 998 interval P2, and their standard uncertainties.

Budget element	Method	P2: Jan 2003 – Aug 2016	
Glaciers	GGM	0.77 ± 0.03	0.77 ± 0.03
Greenland	Altimetry	(0.68 ± 0.06)	
	GGM	(0.21 ± 0.03)	
	Altimetry + GGM	0.89 ± 0.07	
Antarctica	GRACE		0.78 ± 0.02
	Radar altimetry	0.34 ± 0.04	
Land water storage	GRACE		0.27 ± 0.11
	WaterGAP	0.40 ± 0.10	0.40 ± 0.10
Sum of mass contributions		2.40 ± 0.13	2.22 ± 0.15
Ocean mass (global)	GRACE	2.19 ± 0.22	2.19 ± 0.22
Misclosure		-0.21 ± 0.26	-0.04 ± 0.27

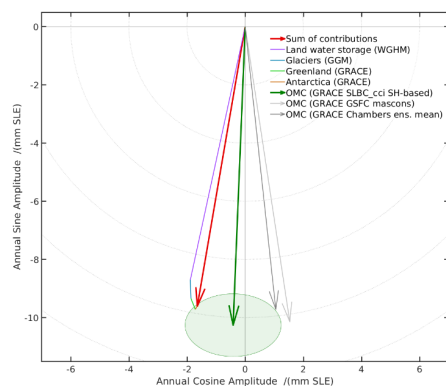
999

1000 4.2 Seasonal component

1001 The inherent monthly resolution of GRACE-based OMC, GRACE-based AIS and GrIS mass changes
 1002 and modelled LWS and glacier mass changes allows us to analyse the budget of the seasonal variations
 1003 of ocean mass. For this purpose, we analyse the annual cosine and sine amplitudes a_3 and a_4 of Eq. (3)
 1004 just in the way we analysed the linear trend a_2 in Sect. 4.1.

1005 Figure 9 shows the results of this analysis. The seasonal amplitudes of GRACE-based OMC and the
 1006 sum of assessed contributions are very similar at 10.3 mm and 9.7 mm, respectively. LWS, with an
 1007 amplitude of 8.9 mm, is by far the dominant source of seasonal OMC. The phase of GRACE OMC is
 1008 approximately 7 days later than the phase of the sum of components. This small offset of phase is within
 1009 the uncertainties assessed for the GRACE OMC results, even though the uncertainty assessment was
 1010 limited to effects of degree-one, C_{20} , and leakage. Errors in the seasonal components of WaterGAP are
 1011 another potential source of the phase offset.

1012 The result does not change significantly (by less than 0.15 mm SLE for the annual cosine and sine
 1013 amplitudes) if we replace the WaterGAP ensemble mean by one of the individual WaterGAP model
 1014 runs or if we replace the ITSG-based GRACE OMC solutions by the CSR-based, GFZ-based, or JPL-
 1015 based SH OMC solution generated by the SLBC_cci project. The phase offset between GRACE OMC
 1016 and the sum of contributions becomes larger if we replace the SLBC_cci OMC solutions by the
 1017 Chambers SH-based OMC solutions or the GSFC mascon solutions (cf. specifications in Sect. 3.3) – see
 1018 grey arrows in Fig. 9.



1019

1020

1021

1022

1023

1024

1025

Figure 9: Phase diagram of annual sine and cosine amplitudes of elements of the ocean-mass budget. Bold red vector: sum of contributions in (using GRACE-based estimates for Greenland and Antarctica). Coloured thin lines: individual contributions (see legend). Bold dark green vector: GRACE ocean-mass change (OMC) SLBC_cci solution based on GRACE ITSG-Grace2018, together with the uncertainty ellipse. Thin grey vectors: external GRACE OMC solutions (GSFC mascons, Chambers' ensemble mean, see legend). The phase difference between the red and the dark green vector corresponds to 7 days.

1026

4.3 Monthly time series

1027

1028

1029

1030

1031

1032

1033

1034

1035

Figure 10 illustrates the monthly-sampled time series of the elements of the OMB. The seasonal signal component, represented by annual and semi-annual harmonic functions was subtracted. The GRACE OMC (dark green line), and the sum of components (dark red line or magenta line) not only have very similar trends (cf. Sect. 4.1). They also reflect interannual variations coherently. These interannual variations overlay the long-term trend and reach amplitudes of 2–3 mm. Clearly, they are dominated by the LWS contribution. They include a minimum in 2007/2008, a maximum in 2010, with a subsequent decrease to a minimum in 2011 related to a La-Niña event (Boening et al., 2012). The sequence continues with an interannual maximum in 2012/2013, a minimum in 2013/2014 and another maximum in 2015/2016.

1036

1037

1038

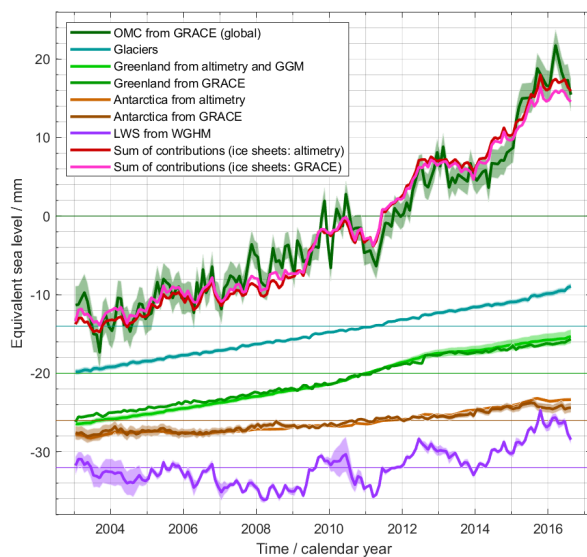
1039

1040

1041

1042

Figure 11a shows the OMB misclosure, together with the combined standard uncertainties of all elements of Eq. (5). The percentages of monthly misclosure values within the 1-sigma, 2-sigma, and 3-sigma combined uncertainty amount to 65.9%, 94.5% and 100.0% for the time series using the GRACE-based ice sheet assessment. Similarly, the percentages are 65.9%, 93.3% and 100.0% for the time series using the altimetry-based ice sheet assessments. These statistics support the realism of the uncertainty assessment where under the assumption of a Gaussian error distribution one would expect 67.3%, 95.5%, and 99.7% of the values to be within the 1-sigma, 2-sigma, and 3-sigma limits, respectively.



1043
1044
1045
1046
1047
1048

Figure 10: Time series of the elements of ocean-mass budget in Jan 2003 – Aug 2016. See legend for attribution of graphs. The GRACE-based time series and the Antarctic altimetry time series were interpolated to monthly sampling. Seasonal variations are subtracted. Each graph shows anomalies with respect to a mean value over 2006–2015. Graphs are shifted arbitrarily along the ordinate axis. Transparent bands show standard uncertainties (except for the red sum-of-contribution graphs).

1049
1050

5 Sea-level budget

1051
1052
1053
1054
1055
1056
1057

We consider the two time periods P1 (altimetry era) and P2 (GRACE/Argo era) as introduced in Sect. 2.2. We concentrate on the steric product generated within SLBC_cci (see Sect. 3.2) when analysing the SLB over P2. For P1, which is not fully covered by the SLBC_cci steric product, we resort to the ensemble mean steric product updated from Dieng et al. (2017). The GRACE-based OMC estimates used here are those evaluated for the ocean between 65°N and 65°S. While for the present results of GRACE OMC this makes little difference, it is consistent to the averaging area of GMSL and the steric component.

1058

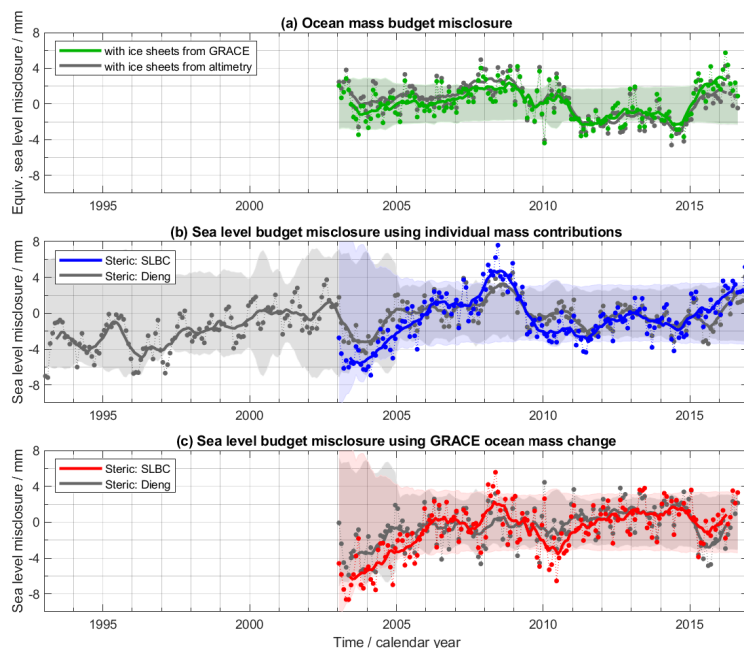
5.1 Linear trend

1059
1060
1061

Linear trends for the elements of the SLB for the two time periods are given in Table 4. The trends were calculated as explained in Sect. 2.2, and uncertainties were assessed as explained in Sect. 2.3 and specified for every element in Sect. 3.

1062
1063

For P1, the observed GMSL trend is $3.05 \pm 0.24 \text{ mm yr}^{-1}$. The sum of individual SLBC_cci v2 components is $2.90 \pm 0.17 \text{ mm yr}^{-1}$. This leaves a misclosure of $0.15 \pm 0.29 \text{ mm yr}^{-1}$.



1064

1065

1066

1067

1068

1069

1070

1071

1072

1073

1074

1075

Figure 11: (a) Ocean-mass budget misclosure (GRACE-based OMC minus sum of assessed contributions) for the time series of monthly anomalies of mass budget elements as shown in Fig. 10. Dots: monthly misclosure for the case of GRACE-based (green) and altimetry-based (grey) ice sheet assessments. Thick lines: running 12-month mean, for better visibility of interannual features. Shaded bands (green and grey, almost identical in the figure): combined standard uncertainty (1-sigma) of the monthly misclosure. (b) Sea-level budget misclosure (GMSL minus sum of contributions) for the time series shown in Fig. 12 using the individual mass contributions (involving the altimetry-based ice sheet assessments). Dots, lines, shaded areas have meanings as in subplot a. Blue and grey: results employing the SLBC_cci Steric data product and the Dieng et al. (2017) ensemble mean dataset, respectively. (c) Same as subplot (b) but with application of GRACE-based OMC, instead of the sum of assessed mass contributions. Red and grey: results employing the SLBC_cci Steric data product and the Dieng et al. (2017) data product, respectively.

1076

1077

1078

1079

1080

1081

1082

1083

1084

1085

For P2, the observed GMSL trend is $3.64 \pm 0.26 \text{ mm yr}^{-1}$. The sum of contributions is $3.37 \pm 0.30 \text{ mm yr}^{-1}$ if OMC is estimated from GRACE. The sum of contributions is $3.59 \pm 0.22 \text{ mm yr}^{-1}$ and $3.41 \pm 0.23 \text{ mm yr}^{-1}$, if the mass contributions are assessed individually, involving altimetry-based estimates or GRACE-based estimates, respectively, for the ice sheets. The three choices of assessing OMC leave misclosures of $0.27 \pm 0.40 \text{ mm yr}^{-1}$, $0.05 \pm 0.34 \text{ mm yr}^{-1}$ and $0.23 \pm 0.35 \text{ mm yr}^{-1}$, respectively. The trend misclosures are hence positive but below the standard uncertainty arising from the combined uncertainties of the involved budget elements.

If we used the Dieng et al. (2017) ensemble mean steric product for the P2 SLB assessment, the trend misclosure remained unchanged, since the steric trend over P2 is equally 1.19 mm yr^{-1} for the two alternative steric products.



1086 **Table 4:** Linear trends of the sea-level budget elements [mm equivalent global mean sea-level per year] for
 1087 the intervals P1 and P2, and their standard uncertainties. The estimates of total sea-level, the steric
 1088 contribution, and the GRACE-based ocean mass contribution refer to the ocean between 65°N and 65°S.

Budget element	Method	P1: Jan 1993	P2:		
		– Dec 2016	Jan 2003 – Aug 2016		
Total sea-level	altimetry	3.05 ± 0.24	3.64 ± 0.26	3.64 ± 0.26	3.64 ± 0.26
Steric component	Dieng	1.15 ± 0.12			
	SLBC_cci + deep steric estimate		1.19 ± 0.17	1.19 ± 0.17	1.19 ± 0.17
Glaciers	GGM	0.64 ± 0.03	0.77 ± 0.03	0.77 ± 0.03	
Greenland	(altimetry)	(0.43 ± 0.04)	(0.68 ± 0.06)		
	(GGM)	(0.17 ± 0.02)	(0.21 ± 0.03)		
Antarctica	Altimetry + GGM	0.60 ± 0.04	0.89 ± 0.07		
	GRACE			0.78 ± 0.02	
	altimetry	0.19 ± 0.04	0.34 ± 0.04		
Land water storage	GRACE			0.27 ± 0.11	
	WaterGAP	0.32 ± 0.10	0.40 ± 0.10	0.40 ± 0.10	
Sum of mass contributions		1.75 ± 0.12	2.40 ± 0.13	2.22 ± 0.15	
Ocean mass (65°N-65°S)	GRACE			2.18 ± 0.25	
Sum of contributions		2.90 ± 0.17	3.59 ± 0.22	3.41 ± 0.23	3.37 ± 0.30
Misclosure		0.15 ± 0.29	0.05 ± 0.34	0.23 ± 0.35	0.27 ± 0.40

1089 The strong limitations of Argo coverage in the years before 2005 are reflected in the uncertainties of the
 1090 SLBC_cci Steric product (Fig. 3). Since the trend calculation accounts for these uncertainties (cf. Sect.
 1091 2.2) the SLBC_cci steric trend is dominated by the data starting from 2005. An alternative accounting
 1092 for the high pre-2005 uncertainties would be to start the entire SLB assessment from 2005. For an
 1093 alternative period Jan 2005 – Aug 2016, the trend budget is given in Table A1 (Appendix). For this
 1094 period, the assessed linear trends of GMSL, the steric component, and the mass component are higher,
 1095 by about 0.16, 0.07 and 0.20–0.29 mm yr⁻¹, than for P2. The conclusions on the budget closure within
 1096 uncertainties remain unchanged.

1097 5.2 Monthly time series

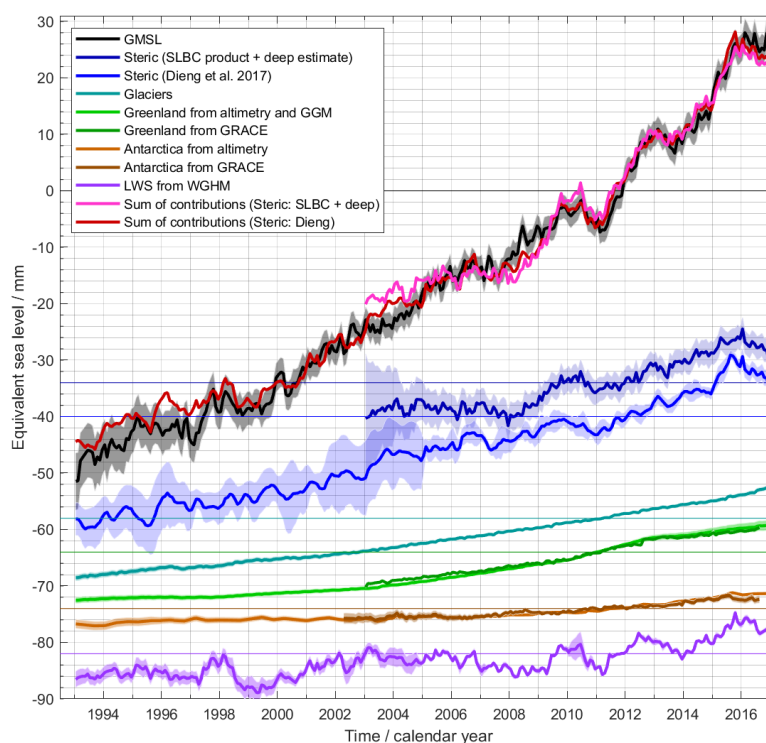
1098 For P1 (altimetry era) our SLB assessment refers to the Dieng et al. (2017) ensemble mean steric product
 1099 and to the mass component composed from the individual contributions (involving altimetry-based
 1100 assessments for the ice sheets). Figure 12 shows the monthly time series of the SLB elements. The
 1101 seasonal signal component is removed. Apart from showing similar linear trends (cf. Sect. 5.1), the
 1102 observed GMSL (black curve) and the sum of contributions (dark red curve) exhibit largely coherent
 1103 interannual variations in the second half of P1 starting from 2005. These interannual variations, overlaid
 1104 on the long-term trend, reach about 3–4 mm amplitudes. As a prominent feature, the La-Niña related
 1105 local GMSL minimum in 2011 (Boening et al., 2012) arises as a superposition of synchronous variations
 1106 of a LWS effect and a steric effect.

1107 The associated misclosure time series are shown in Fig. 11b (in grey). Deviations between GMSL and
 1108 the sum of components are relatively large in the early years 1993–1996. In this period GMSL
 1109 uncertainties are large (cf. Fig. 1b) due to uncertainties of the TOPEX-A drift correction. In addition,
 1110 the steric component has large uncertainties in this period and further through 2004, where it is based



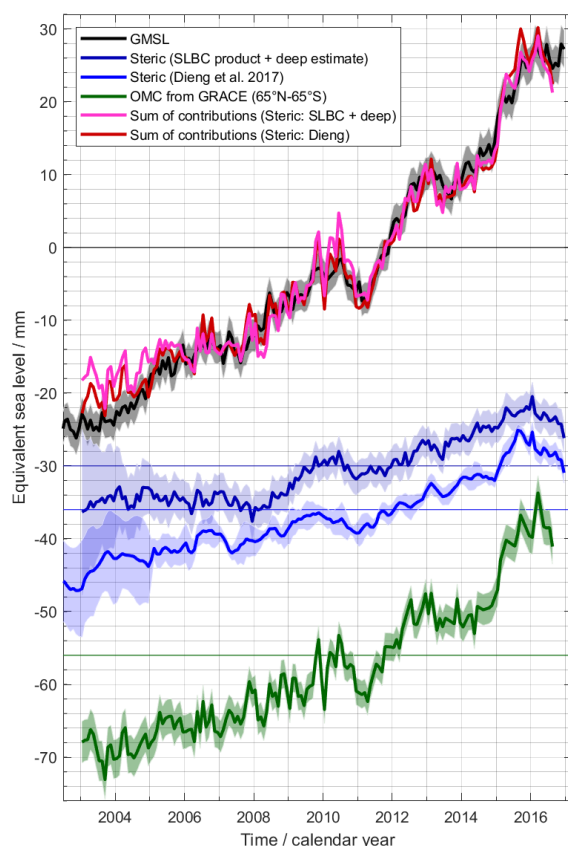
1111 on XBT data and therefore suffers from sparse coverage both geographically and at depth (below 700
1112 m). The monthly misclosure values for P1 are within the 1-sigma and 2-sigma uncertainty band,
1113 respectively, for 90.9% and 100.0% of the months. Hence, the misclosure has a narrower distribution
1114 than allowed for by the assessed uncertainties.

1115 For P2 (GRACE/Argo era) the SLB analysis may employ the SLBC_cci steric dataset, which is also
1116 shown in Fig. 12. Again, interannual variations of GMSL (black curve) and the sum-of-components
1117 (magenta curve) agree largely in their sequence of positive and negative deviations from a long-term
1118 evolution, with the exception of the early Argo years 2003 and 2004. Figure 11b shows (in blue) the
1119 misclosure of the SLB when using this SLBC_cci steric dataset (and the individual mass contribution
1120 assessments). The percentage of misclosures within the 1-sigma, 2-sigma and 3-sigma ranges of
1121 combined uncertainties are 84.8%, 99.4%, and 100.0%, respectively.



1122

1123 **Figure 12:** Time series of SLB elements involving the individual contributions to ocean-mass change. See
1124 legend for attribution of graphs. The sum-of-components graphs use altimetry-based ice sheet assessments.
1125 The GRACE-based time series and the Antarctic altimetry time series were interpolated to monthly
1126 sampling. Seasonal variations are subtracted. Each graph shows anomalies with respect to a mean value
1127 over 2006–2015. Graphs are shifted arbitrarily along the ordinate axis. Standard uncertainties are shown by
1128 transparent bands (except for the sum-of-contribution graphs).



1129

1130 **Figure 13:** Time series of SLB elements involving the GRACE-based assessment of ocean-mass change.
1131 See legend for attribution of graphs. The GRACE-based time series were interpolated to monthly sampling.
1132 Seasonal variations are subtracted. Each graph shows anomalies with respect to a mean value over 2006–
1133 2015. Graphs are shifted arbitrarily along the ordinate axis. Standard uncertainties are shown by transparent
1134 bands (except for the sum-of-contribution graphs).

1135 For the case of using the GRACE-based OMC, the monthly budget assessment over P2 is illustrated in
1136 Fig. 13. While the use of GRACE OMC introduces more month-to-month noise into the sum-of-
1137 components time series than the use of individual mass contributions, the features of interannual
1138 variations discussed above are again coherently reflected in the GMSL and the sum of-contributions.
1139 The related monthly misclosure time series are shown in Fig. 11c. When using the SLBC_cci steric
1140 product, the monthly misclosure values are within the 1-sigma, 2-sigma, and 3-sigma
1141 range, respectively, for 89.6%, 100.0% and 100.0% of the months.



1142 6 Attribution of misclosure

1143

1144 We cannot attribute the misclosures in the budgets of linear trends, as the uncertainties on the order of
1145 0.3 mm yr^{-1} in various elements of the OMB and SLB would make such an attribution extremely
1146 ambiguous. In contrast, for the interannual features in the misclosure time series of the different budgets
1147 (Fig. 11) we can suggest indications on misclosure origins by comparing them among each other and
1148 with the interannual variations of the budget elements. Interannual variations are depicted as variations
1149 of the running annual means of the misclosure time series, shown as bold curves in Fig. 11.

1150 The OMB misclosure varies interannually between roughly -2 mm and $+2 \text{ mm}$ (bold curves in Fig. 11a).
1151 The SLB misclosure varies interannually between roughly -6 mm and $+4 \text{ mm}$ (bold curves in Fig. 11b,
1152 c) depending on which steric product and which way of estimating OMC are used. Errors of the datasets
1153 on GMSL, the steric contribution, GRACE-based OMC, and LWS are most likely responsible for these
1154 interannual misclosures. The glaciers and ice sheets time series involve relatively small interannual
1155 variations (cf. Fig. 12) so that their errors are unlikely to exceed the sub-millimetre level. The unassessed
1156 atmospheric water content contribution (cf. Sect. 3.8) could add to the misclosure, though.

1157 As a starting point, we discuss the SLB misclosure obtained if estimating the steric contribution by the
1158 SLBC_cci steric product and estimating the mass component by the sum of mass contributions (Fig. 11b,
1159 blue curve). As a first feature, the misclosure moves from -6 mm to 0 mm between mid-2003 and mid-
1160 2006, indicating that over this 3-year period the sum of contributions rose 2 mm yr^{-1} less than the
1161 altimetry-based GMSL. At least part of this feature is readily explained by the limitations of the
1162 SLBC_cci steric product in these early years of the Argo system, as discussed in Sect. 3.2.

1163 As a second prominent feature, the misclosure rises by 4 mm from 2006 to 2008 and falls again by 6 mm
1164 from 2008 and 2010. From Fig. 12 we see that this misclosure is related to the fact that the sum of
1165 components suggests a temporary slowdown of sea-level rise from 2006 to 2008, while the altimetric
1166 GMSL exhibits less of such a slowdown. The SLBC_cci steric time series (Fig. 3, 12) has a feature of
1167 fall and rise by $3\text{--}4 \text{ mm}$ in those 2006–2008 and 2008–2010 periods, and this feature enters the SLB
1168 misclosure with negative sign. In addition, the mass budget misclosure (Fig. 11a) has a similar rise and
1169 fall by 1 to 2 mm in the same 2006–2008 and 2008–2010 periods. Replacing the individual mass
1170 components by GRACE-based OMC reduces the misclosure feature (compare Fig. 11b blue line and
1171 Fig. 11c red line). Replacing the SLBC_cci steric product by the Dieng et al. (2017) ensemble mean
1172 steric time series further reduces this feature (compare Fig. 11c red line and grey line). This may suggest
1173 that between 2006 and 2010 the interannual variations of OMC and the steric component are more
1174 accurately represented by GRACE-based OMC and the Dieng ensemble mean, respectively, than by the
1175 sum of mass contributions involving modelled LWS and the SLBC_cci steric product.



1176 **7 Discussion**

1177 **7.1 Budget closure and uncertainties**

1178 In all our budget assessments for linear trends, the misclosure is within the 1-sigma range of the
1179 combined uncertainties of the budget elements. As a consequence, no statistically significant estimates
1180 of missing budget elements can be made based on the present budget assessments. Assessed
1181 uncertainties of the trends of various budget elements are on a similarly high level. For example, for P2
1182 the trend uncertainties are 0.26 mm yr^{-1} for GMSL, 0.17 mm yr^{-1} for the steric component, and 0.13
1183 mm yr^{-1} to 0.25 mm yr^{-1} for the mass component, depending on how it is assessed. This prevents us
1184 from validating the linear trend of any single component through budget considerations. For example,
1185 we cannot easily use budget considerations to decide which GRACE-based OMC trend in Table 1 is
1186 most accurate. In cases where the budget of trends is closed much better than the combined uncertainties
1187 (e.g., the second data columns in Table 3 and Table 4), this could just result from an incidental
1188 compensation of errors in the involved budget elements.

1189 The trends of the individual budget components assessed here for P1 and P2 agree within stated
1190 uncertainties with the trends of the same budget components assessed by the IPCC SROCC
1191 (Oppenheimer et al., 2019, Table 4.1) for the periods 1993–2015 and 2006–2015, respectively, even if
1192 differences between the considered periods may add to the differences between the two assessments.
1193 The single exception from this agreement applies to the LWS contribution. While SROCC reports a
1194 negative sea-level contribution at -0.21 mm yr^{-1} for 2006–2015 based on GRACE analyses, our
1195 WaterGAP results indicate a positive contribution at 0.65 mm yr^{-1} for 2006–2015 (0.40 mm yr^{-1} for P2).
1196 However, a new GRACE-based assessment of continental mass change (Cáceres et al., 2020, updated
1197 by Gutknecht et al., 2020; cf. Sect. 3.8) corrected for the GGM-based glacier mass trend also determines
1198 a positive LWS contribution at 0.31 mm yr^{-1} for 2006–2015 (0.42 mm yr^{-1} for P2), consistent with the
1199 WaterGAP results. Assessing the LWS contribution to GMSL remains a challenge.

1200 Our analysis of the OMB and the SLB on a time series basis exploits the intrinsic monthly resolution of
1201 almost all budget elements. Only for the altimetry-based GrIS and AIS assessments, true month-to-
1202 month variability is not contained in the time series interpolated to monthly resolution. We found that
1203 the spread of monthly misclosure of OMB and of SLB is similar to, or narrower than, a Gaussian
1204 distribution with a standard deviation equal to the combined standard uncertainties of the budget
1205 elements.

1206 **7.2 Limitations of the study**

1207 While the uncertainty assessments made for the individual budget components were described in a
1208 common framework, different approaches to uncertainty characterisation were used for the different
1209 products. The reasons for the conceptual differences as well as their consequences for the relative
1210 uncertainty levels within the budget assessments have not been fully elaborated. A further consolidation
1211 and standardisation of uncertainty characterisation could allow, in a more flexible way, to propagate



1212 uncertainties to different functionals, such as to anomalies with respect to different reference states, or
1213 to time-dependent rates of change.

1214 No correlation between errors of different budget elements were accounted for when combining the
1215 different elements in budget assessments. However, such correlations exist. An important example is
1216 the GIA correction, which is significant by its magnitudes and uncertainties. Errors in the GIA
1217 corrections for GRACE OMC estimates ($-1.37 \pm 0.17 \text{ mm yr}^{-1}$) are likely correlated with errors of GIA
1218 corrections for GRACE inferences of the ice-sheet contribution ($-0.14 \pm 0.09 \text{ mm yr}^{-1}$ for Antarctica; $-$
1219 $0.02 \pm 0.02 \text{ mm yr}^{-1}$ for Greenland) and also correlated with the error of the GIA correction applied to
1220 altimetric sea-level change ($-0.30 \pm 0.05 \text{ mm yr}^{-1}$).

1221 As a matter of fact, already the choice of a GIA model used for GIA corrections poses consistency issues
1222 not resolved in the present study. We used the regional GIA model IJ05_R2 (Ivins et al., 2013) for
1223 GRACE-based AIS mass change estimates as opposed to the global GIA models used for GRACE-based
1224 OMC estimates and GrIS mass change estimates. It is subject to ongoing controversy whether global
1225 models are consistent with geodetic and geological evidence over Antarctica (Ivins et al., 2013; Argus
1226 et al., 2014). Regional GIA models like IJ05_R2, W12 (Ivins et al., 2013; Whitehouse et al., 2012), on
1227 the other hand, are not constructed to obey geological evidence on global sea-level history.

1228 Contributions discussed in Sect. 3.8 that were not included in our budget analysis nor in our uncertainty
1229 assessment are on the order of 0.1 mm yr^{-1} , with the largest single unconsidered contribution likely
1230 being the elastic seafloor deformation effect.

1231 It is also important to mention that our ‘global’ mean sea level assessment as well as our assessment of
1232 the steric contribution, by its limitation to the 65°N – 65°S latitude range, left out 6% of the global ocean
1233 in the Arctic and in the Southern Ocean. In the polar oceans, satellite altimetry has sampling limitations
1234 due to orbital geometry and sea-ice coverage. Likewise, Argo floats and other in-situ sensors have
1235 sampling limitations due to the presence of sea ice. Therefore, SLB assessments for the polar oceans
1236 (e.g., Raj et al., 2020) are even more challenging than for the 65°N – 65°S latitude range focussed on in
1237 this paper. An assessment of the truly global mean sea-level and its contributions would involve higher
1238 uncertainties than quoted here for the 65°N – 65°S range.

1239 8 Data availability

1240 A compiled dataset of time series of the elements of the GMSL budget and of the OMB together with
1241 their uncertainties, are freely available for download at
1242 <https://doi.org/10.5285/1562578dd07844f19f01f0db9366106d> (Horwath et al., 2021). The single file in
1243 csv format contains the time series presented in Fig. 10, 12 and 13. These time series are all at an
1244 identical monthly sampling, resulting from interpolation of the original time series where necessary.
1245 Uncertainties were partly recalculated from the original data products (as described in Sect. 3) in order
1246 to make them consistently refer to anomalies with respect to the same reference interval Jan 2006 – Dec
1247 2015 as stated in Sect. 2.3. Seasonal signals are removed from all time series.



1248 **9 Conclusions and outlook**

1249 This study assessed CCI data products related to the SLB, advanced the generation of new time series
1250 of SLB elements based on satellite earth observation and modelling, and integrated, within a consistent
1251 framework, the products into an analysis of the OMB and the SLB. The consolidation, improvement,
1252 and exhibition (in Fig. 1, 3–8) of the uncertainty characterization for every budget element were central
1253 to this study. The datasets and analyses presented here document both achievements and limitations
1254 identified within the SLBC_cci study.

1255 **9.1 Advances on data products on individual budget elements**

1256 For the GMSL, the use of the averaged ESA CCI 2.0 gridded sea-level data was enhanced by the
1257 incorporation of the uncertainty estimate over each GMSL time step from Ablain et al. (2019). Three
1258 major sources of errors were considered in the composition of a variance-covariance matrix to obtain
1259 GMSL uncertainty. The GMSL trend uncertainty over 1993–2016 (after correcting the TOPEX A drift)
1260 is assessed as 0.24 mm yr^{-1} (1-sigma).

1261 For the steric sea-level change, we developed a formal uncertainty framework around the estimation of
1262 steric height from Argo profiles, including propagation to gridded and time series products. The
1263 framework includes simple models to estimate each uncertainty source and their error covariance
1264 structures. Global sampling uncertainty was included when obtaining the global mean from the gridded
1265 products. Inclusion of SST from SST CCI to condition the climatology of the mixed layer reduced bias
1266 of the steric change in the upper ocean, with a small beneficial impact. A full error covariance matrix
1267 was calculated for the global steric time series, facilitating robust calculation of linear trends and their
1268 uncertainties.

1269 OMC was inferred from recent GRACE SH solution releases. The choice of methodology built on
1270 comprehensive insights into the sensitivity to choices of input data and to choices of the treatment of
1271 background models.

1272 For the glacier contribution, the introduction of an ensemble approach to reconstruct glacier mass change
1273 and the systematic multi-objective optimisation of the global model parameters led to results that
1274 generally confirm the previous estimates, and which also agree well with methods based on observations
1275 only (Zemp et al., 2019). However, the increased model performance (higher correlation with
1276 observations on individual glaciers, better representation of the observed variance of mass balance)
1277 increased the confidence in the results.

1278 For the GrIS contribution, we devised an empirical and effective way to convert the radar altimetry
1279 elevation changes into mass changes. The resulting time series was independently tested against the
1280 GRACE-derived time series and it has shown very high compatibility.

1281 For the AIS contribution, the new time series of Antarctica mass change from satellite radar altimetry is
1282 the result of an improved processing chain and a better characterisation of uncertainties. With a time-
1283 evolving ice and snow density mask and a new method for interpolating surface elevation change in
1284 areas located beyond the latitudinal limit of satellite radar altimeters and in between satellite tracks, we



1285 have provided an updated time series of Antarctica mass change from 1992 to 2017 revealing that ice
1286 losses at Pine Island and Thwaites Glaciers basins are about 6 times greater than at the start of our
1287 survey.

1288 For the LWS contribution, the version of the global hydrological model WaterGAP (version 2.2d) was
1289 developed and applied, which includes the commissioning years of individual reservoirs to take into
1290 account increased water storage behind dams as well as regionalised model parameterisations to improve
1291 the simulation of groundwater depletion (Müller Schmied et al., 2021). Comprehensive insights into
1292 the model sensitivity to choices of irrigation water use assumptions and climate input data were acquired,
1293 enabling a first uncertainty estimation. The good fit of simulated monthly total water storage anomaly
1294 (sum of land water storage and glacier storage) to GRACE-derived estimates, in particular regarding
1295 seasonality and de-seasonalised long-term variability, enhanced the confidence in the simulated land
1296 water contributions (Cáceres et al., 2020).

1297 **9.2 Sea-level budget and ocean-mass budget**

1298 As summarized in Table 3 and Table 4, the SLB and the OMB are closed within uncertainties for their
1299 evaluation periods P1 and P2 (SLB) and P2 (OMB). We may reformulate the budgets as follows. The
1300 GMSL linear trend over P1 and P2 is 3.05 mm yr^{-1} and 3.64 mm yr^{-1} , respectively. The larger trend
1301 over P2 than over P1 is due to an increased mass component, predominantly from Greenland but also
1302 from the other mass contributors. Over P1 (P2) the steric contribution is 38% (33%) of GMSL rise,
1303 while the mass contribution is 57% (60%–66%). Among the sources of OMC, glaciers outside
1304 Greenland and Antarctica contributed 21% (21%) of total GMSL rise; Greenland contributed 20%
1305 (21%–24%); Antarctica contributed 6% (8%–9%); and LWS contributed 10% (11%). The SLB
1306 misclosure (GMSL minus sum of assessed contributions) is between +1% and +7% of GMSL rise.
1307 Ranges quoted here arise from different options of assessing the contributions. Uncertainties given in
1308 Table 3 and 4 are not repeated here.

1309 We cannot attribute the statistically insignificant misclosure of linear trends. We tentatively attributed
1310 interannual features of misclosure to errors in some of the involved datasets. When the SLBC_cci steric
1311 product is used which uses constraints towards a static climatology, a SLB misclosure in the early years
1312 of Argo 2003–2006 is likely due to an underestimation of the steric sea-level rise. An interannual
1313 misclosure feature between 2006 and 2010 might be related to the SLBC_cci steric product and the
1314 WaterGAP model making the impression of a temporary slowdown in sea-level rise in 2006–2008 with
1315 subsequent recovery in 2008–2010, which is not as pronounced in the GMSL record.

1316 **9.3 Outlook**

1317 Future work will naturally include the extension of the considered time periods. It will be additionally
1318 spurred by the availability of new data types (Cazenave et al., 2019). GRACE-FO launched in August
1319 2018 already facilitates a satellite gravity times series spanning 19 years (yet with interruptions). It will
1320 be equally important to continue this time series beyond GRACE-FO as currently jointly considered by
1321 ESA and NASA for the next generation gravity mission (Haagmans et al., 2020). The Deep Argo project



1322 (Roemmich et al., 2019) promises new observational constraints on deep ocean steric contributions.
1323 With the Sentinel-6/Jason-CS mission (Scharroo et al., 2016) the continuation of satellite altimetry in
1324 the 66°N–66°S latitude range is enabled with synthetic aperture resolution capabilities exceeding those
1325 of pulse-limited altimeters. Continuity of precise satellite radar altimetry at high latitudes beyond
1326 CryoSat-2 still has to be ensured. Perspectives and requirements for long-term GMSL budget studies
1327 are detailed by Cazenave et al. (2019). Additional ECVs related to the global water and energy cycle
1328 call for their exploration in SLB studies. In the framework of ESA’s CCI, results from Water Vapour
1329 CCI, Snow CCI, or Lakes CCI are among the candidates.

1330 Limitations discussed in Sect. 7.2 call for further methodological developments. For example, the
1331 consideration of GIA as an own element in SLB analyses could help to enforce its consistent treatment.
1332 This will be particularly important for regional SLB studies, since GIA is a driver of regional sea-level
1333 change and OMC. Such a treatment of GIA could be in accord with the treatment of elastic solid-Earth
1334 load deformations as proposed by Vishwakarma et al. (2020). Recent probabilistic characterizations of
1335 GIA model errors (Caron et al., 2018) allow their propagation to error covariances of the SLB elements,
1336 an approach not yet realized.

1337 While GMSL is an important global indicator, it is indispensable to monitor and understand the
1338 geographic patterns of sea-level change, that is, regional sea-level. Regional sea-level reflects the
1339 different processes causing sea-level change, which may be hidden in GMSL (e.g., Stammer et al., 2013;
1340 Hamlington et al., 2020). Understanding and projecting these processes, with implications down to
1341 coastal impact research, is the ultimate goal. The further development of methodologies for regional
1342 SLB assessments and their application will be an important step towards this goal.

1343 **Author contributions**

1344 AC, JB, MH, AS, RF, CJM, JAJ, OBA, BM, FP, PD, KN designed the study. MH led the study and the
1345 compilation and editing of the manuscript. AC, HKP, FM contributed the GMSL dataset and its
1346 description. CJM, CRM, KvS contributed the SLBC_cci steric dataset and its description. BDG
1347 contributed the GRACE-based OMC dataset and its description. BM contributed the global glacier
1348 dataset and its description. VRB, RF contributed the GRACE-based Greenland dataset and its
1349 description. LSS, SBS contributed the altimetry-based Greenland dataset and its description. AR, MH
1350 contributed the GRACE-based Antarctica dataset and its description. AEH, AS, IO contributed the
1351 altimetry-based Antarctica dataset and its description. PD, DC, HMS contributed the LWS dataset and
1352 its description. BDG conducted the ocean mass budget analyses and drafted their description. HKP, AC,
1353 MH conducted the sea level budget analyses and misclosure attribution study and drafted their
1354 description. All authors discussed the results and contributed to the editing of the manuscript. KN
1355 managed the project administration. JB launched the ESA CCI Sea Level Budget Closure Project
1356 (SLBC_cci) and, with the support of MR, supervised the development of this research activity and
1357 reviewed all the deliverables.



1358 **Competing interests**

1359 The authors declare that they have no conflict of interest.

1360 **Acknowledgements**

1361 This study was supported by the European Space Agency through the Climate Change Initiative project
 1362 CCI Sea-level Budget Closure (contract number 4000119910/17/I-NB). We thank the German Space
 1363 Operations Center (GSOC) of the German Aerospace Center (DLR) for providing continuously and
 1364 nearly 100% of the raw telemetry data of the twin GRACE satellites.

1365 **Appendix A**

1366 **Table A1:** Same as the last three columns of Table 4, but for the alternative period Jan 2005 – Aug 2016, when
 1367 the Argo network was fully established. Linear trends of the sea-level budget elements [mm equivalent global
 1368 mean sea-level per year].

Budget element	Method	Jan 2005 – Aug 2016		
Total sea-level	altimetry	3.80 ± 0.28	3.80 ± 0.28	3.80 ± 0.28
Steric component				
	SLBC_cci + deep steric estimate	1.26 ± 0.17	1.26 ± 0.17	1.26 ± 0.17
Glaciers	GGM	0.78 ± 0.04	0.78 ± 0.04	
Greenland	(altimetry)	(0.72 ± 0.07)		
	(GGM)	(0.20 ± 0.03)		
Antarctica	Altimetry + GGM	0.92 ± 0.08		
	GRACE		0.81 ± 0.02	
	altimetry	0.42 ± 0.04		
Land water storage	GRACE		0.31 ± 0.11	
	WaterGAP	0.57 ± 0.10	0.57 ± 0.10	
Sum of mass contributions		2.69 ± 0.14	2.47 ± 0.15	
Ocean mass (65°N-65°S)	GRACE		2.38 ± 0.25	
Sum of contributions		3.94 ± 0.22	3.73 ± 0.23	3.63 ± 0.30
Misclosure		-0.14 ± 0.36	0.07 ± 0.36	0.17 ± 0.41

1369

1370 **References**

1371 A, G., Wahr, J., and Zhong, S.: Computations of the viscoelastic response of a 3-D compressible Earth to surface
 1372 loading: an application to Glacial Isostatic Adjustment in Antarctica and Canada, *Geophys. J. Int.*, 192, 557–
 1373 572, <https://doi.org/10.1093/gji/ggs030>, 2013.
 1374 Ablain, M., Cazenave, A., Larnicol, G., Balmaseda, M., Cipollini, P., Faugère, Y., Fernandes, M. J., Henry, O.,
 1375 Johannessen, J. A., Knudsen, P., Andersen, O., Legeais, J., Meyssignac, B., Picot, M., Roca, M., Rudenko, S.,
 1376 Scharffenberg, M. G., Stammer, D., Timms, G., and Benveniste, J.: Improved sea-level record over the satellite
 1377 altimetry era (1993–2010) from the climate change Initiative project, *Ocean Sci.*, 11, 67–82,
 1378 <https://doi.org/10.5194/os-11-67-2015>, 2015.
 1379 Ablain, M., Legeais, J. F., Prandi, P., Marcos, M., Fenoglio-Marc, L., Dieng, H. B., Benveniste, J., and Cazenave,
 1380 A.: Altimetry-based sea-level at global and regional scales, *Surv. Geophys.*, 38, 7–31,
 1381 <https://doi.org/10.1007/s10712-016-9389-8>, 2017a.
 1382 Ablain, M., Jugier, R., Zawadki, L., Taburet, N., Cazenave, A., & Meyssignac, B.: The TOPEX-A Drift and
 1383 Impacts on GMSL Time Series, AVISO Website, October 2017,
 1384



- 1385 https://meetings.aviso.altimetry.fr/fileadmin/user_upload/tx_ausycslseminar/files/Poster_OSTST17_GMSL_
1386 [Drift_TOPEX-A.pdf](#), 2017b .
- 1387 Ablain, M., Meyssignac, B., Zawadzki, L., Jugier, R., Ribes, A., Spada, G., Cazenave A., Picot, N.: Uncertainty
1388 in satellite estimates of global mean sea-level changes, trend and acceleration Earth Syst. Sci. Data, 11(3),
1389 1189–1202, <https://doi.org/10.5194/essd-11-1189-2019>, 2019.
- 1390 Argus D., Peltier W., Drummond R., and Moore S.: The Antarctic component of glacial isostatic adjustment model
1391 ICE-6G_C (VM5a) based upon GPS measurements of vertical motion of the crust, exposure age dating of ice
1392 thickness variations and relative sea-level histories, *Geophys. J. Int.*, 198(1), 537–563,
1393 <https://doi.org/10.1093/gji/ggu140>, 2014.
- 1394 Bamber, J. L., Westaway, R. M., Marzeion, B., and Wouters, B.: The land ice contribution to sea-level during the
1395 satellite era, *Environ. Res. Lett.*, 13(6), 063008, <https://doi.org/10.1088/1748-9326/aac2f0>, 2018.
- 1396 Barletta, V. R., Sørensen, L. S., and Forsberg, R.: Scatter of mass changes estimates at basin scale for Greenland
1397 and Antarctica, *The Cryosphere*, 7(5), 1411–1432, <https://doi.org/10.5194/tc-7-1411-2013>, 2013.
- 1398 Bergmann-Wolf, I., Zhang, L. and Dobsław, H. (2014). Global Eustatic Sea-Level Variations for the
1399 Approximation of Geocenter Motion from Grace, *J. Geodetic Sci.*, 4(1), doi:10.2478/jogs-2014-0006, 2014.
- 1400 Blazquez, A., Meyssignac, B., Lemoine, J. M., Berthier, E., Ribes, A., & Cazenave, A.: Exploring the uncertainty
1401 in GRACE estimates of the mass redistributions at the Earth surface: implications for the global water and sea-
1402 level budgets, *Geophys. J. Int.*, 215(1), 415–430, <https://doi.org/10.1093/gji/ggy293>, 2018.
- 1403 Boening, C., Willis, J. K., Landerer, F. W., Nerem, R. S., & Fasullo, J.: The 2011 La Niña: So strong, the oceans
1404 fell, *Geophys. Res. Lett.*, 39(19), L19602, doi:10.1029/2012GL053055, 2012.
- 1405 Bojinski, S., Verstraete, M., Peterson, T. C., Richter, C., Simmons, A., and Zemp, M.: The concept of essential
1406 climate variables in support of climate research, applications, and policy, *Bull. Am. Meteorol. Soc.*, 95(9),
1407 1431–1443, <https://doi.org/10.1175/BAMS-D-13-00047.1>, 2014.
- 1408 Cáceres, D., Marzeion, B., Malles, J. H., Gutknecht, B., Müller Schmied, H., and Döll, P.: Assessing global water
1409 mass transfers from continents to oceans over the period 1948–2016, *Hydrol. Earth Syst. Sci.* 24, 4831–4851,
1410 <https://doi.org/10.5194/hess-24-4831-2020>, 2020.
- 1411 Caron, L., Ivins, E. R., Larour, E., Adhikari, S., Nilsson, J., and Blewitt, G.: GIA model statistics for GRACE
1412 hydrology, cryosphere, and ocean science, *Geophys. Res. Lett.*, 45, 2203–2212,
1413 <https://doi.org/10.1002/2017GL076644>, 2018.
- 1414 Cazenave, A., Hamlington, B., Horwath, M., Barletta, V., Benveniste, J., Chambers, D., Döll, P., Hogg, A. E.,
1415 Legeais, J. F., Merrifield, M., Meyssignac, B., Mitchum, G., Nerem, S., Pail, R., Palanisamy, H., Paul, F., von
1416 Schuckmann, K., Thompson, Ph.: Observational requirements for long-term monitoring of the global mean sea
1417 level and its components over the altimetry era, *Front. Marine Sci.*, 6, 582,
1418 <https://doi.org/10.3389/fmars.2019.00582>, 2018.
- 1419 Chambers D., Wahr J., Tamisiea M., and Nerem, R.: Ocean mass from GRACE and glacial isostatic adjustment, *J.*
1420 *Geophys. Res. Solid Earth*, 115(B11), <https://doi.org/10.1029/2010JB007530>, 2010.
- 1421 Chambers D. P., Cazenave A., Champollion N., Dieng H., Llovel, W., Forsberg R., von Schuckmann, K., and Wada
1422 Y.: Evaluation of the global mean sea-level budget between 1993 and 2014. *Surv. Geophys.*, 38(1), 309–327,
1423 <https://doi.org/10.1007/s10712-016-9381-3>, 2017.
- 1424 Chen, X., Zhang, X., Church, J. A., Watson, C. S., King, M. A., Monselesan, D., Legresy, B., and Harig, C.: The
1425 increasing rate of global mean sea-level rise during 1993–2014, *Nat. Clim. Change*, 7, 492–495,
1426 doi:10.1038/nclimate3325, 2017.
- 1427 Chen, J., Tapley, B., Wilson, C., Cazenave, A., Seo, K.-W., & Kim, J.-S.: Global ocean mass change from GRACE
1428 and GRACE follow-on and altimeter and Argo measurements. *Geophys. Res. Lett.*, 47, e2020GL090656,
1429 <https://doi.org/10.1029/2020GL090656>, 2020.
- 1430 Cheng, M. K., Tapley, B. D., and Ries, J. C.: Deceleration in the Earth's oblateness, *J. Geophys. Res.*, V118, 1–8,
1431 <https://doi.org/10.1002/jgrb.50058>, 2013.
- 1432 Church, J. A., Clark, P. U., Cazenave, A., Gregory, J. M., Jevrejeva, S., Levermann, A., Merrifield, M. A., Milne,
1433 G. A., Nerem, R. S., Nunn, P. S., Payne, A. J., Pfeffer, W. T., Stammer, D., and Unnikrishnan A. S.: Sea-level
1434 Change. In: *Climate Change 2013: The Physical Science Basis. Contribution of Working Group I to the Fifth*
1435 *Assessment Report of the Intergovernmental Panel on Climate Change*. Cambridge University Press,
1436 Cambridge, United Kingdom and New York, NY, USA, 2013.
- 1437 Compo, G. P., Whitaker, J. S., Sardeshmukh, P. D., Matsui, N., Allan, R. J., Yin, X., Gleason, B. E., Vose, R. S.,
1438 Rutledge, G., Bessemoulin, P., and Brönnimann, S.: The twentieth century reanalysis project, *Quarterly Journal*
1439 *of the Royal Meteorological Society*, 137(654), 1–28, <https://doi.org/10.1002/qj.776>, 2011.
- 1440 Dee, D. P., Uppala, S. M., Simmons, A. J., Berrisford, P., Poli, P., Kobayashi, S., Andrae, U., Balmaseda, M. A.,
1441 Balsamo, G., Bauer, P., Bechtold, P., Beljaars, A. C. M., van de Bert, L., Bidlot, J., Bormann, N., Delsol, C.,
1442 Dragani, R., Fuentes, M., Geer, A. J., Haimberger, L., Healy, S. B., Hersbach, H., Hólm, E. V., Isaksen, L.,
1443 Källberg, P., Köhler, M., Matricardi, M., McNally, A. P., Monge-Sanz, B. M., Morcrette, J.-J., Park, B.-K.,
1444 Peubey, C., de Rosnay, P., Tavolato, C., Thépaut, J.-M., and Vitart, F.: The ERA-Interim reanalysis:



- 1445 Configuration and performance of the data assimilation system, *Q. J. Roy. Meteor. Soc.*, 137(656), 553–597,
1446 <https://doi.org/10.1002/qj.828>, 2011.
- 1447 Dieng, H.B., A. Cazenave, B. Meyssignac, and M. Ablain: New estimate of the current rate of sea-level rise from
1448 a sea-level budget approach, *Geophys. Res. Lett.*, 44, doi:10.1002/2017GL073308, 2017.
- 1449 Dobslaw, H., Flechtner, F., Bergmann-Wolf, I., Dahle, C., Dill, R., Esselborn, S., Sasgen, I., and Thomas, M.:
1450 Simulating high-frequency atmosphere-ocean mass variability for dealiasing of satellite gravity observations:
1451 AOD1B RL05, *J. Geophys. Res.: Oceans*, 118(7), 3704–3711. <https://doi.org/10.1002/jgrc.20271>, 2013.
- 1452 Dobslaw, H., Bergmann-Wolf, I., Dill, R., Forootan, E., Klemann, V., Kusche, J., and Sasgen, I.: The updated ESA
1453 Earth System Model for future gravity mission simulation studies, *J. Geod.*, 89, 5, 505–513,
1454 <https://doi.org/10.1007/s00190-014-0787-8>, 2015.
- 1455 Döll, P., Fiedler, K., Zhang, J.: Global-scale analysis of river flow alterations due to water withdrawals and
1456 reservoirs, *Hydrol. Earth Syst. Sci.*, 13(12), 2413, <https://doi.org/10.5194/hess-13-2413-2009>, 2009.
- 1457 Döll, P., Kaspar, F., Lehner, B.: A global hydrological model for deriving water availability indicators: model
1458 tuning and validation, *J. Hydrol.*, 270(1–2), 105–134, [https://doi.org/10.1016/S0022-1694\(02\)00283-4](https://doi.org/10.1016/S0022-1694(02)00283-4), 2003.
- 1459 Döll, P., Douville, H., Güntner, A., Müller Schmied, H., and Wada, Y.: Modelling Freshwater Resources at the
1460 Global Scale: Challenges and Prospects, *Surv. Geophys.* 37 (2), 195–221, <https://doi.org/10.1007/s10712-015-9343-1>, 2016.
- 1462 Döll, P., and Lehner, B.: Validation of a new global 30-min drainage direction map, *J. Hydrol.*, 258(1–4), 214–
1463 231, [https://doi.org/10.1016/S0022-1694\(01\)00565-0](https://doi.org/10.1016/S0022-1694(01)00565-0), 2002.
- 1464 Döll, P., Müller Schmied, H., Schuh, C., Portmann, F. T., and Eicker, A.: Global-scale assessment of groundwater
1465 depletion and related groundwater abstractions: Combining hydrological modeling with information from well
1466 observations and GRACE satellites, *Water Resour. Res.* 50 (7), 5698–5720.
1467 <https://doi.org/10.1002/2014WR015595>, 2014.
- 1468 Flechtner, F., Dobslaw, H., and Fagiolini, E.: AOD1B product description document for product release 05 (Rev.
1469 4.2, May 20, 2014), Technical Note, GFZ German Research Centre for Geosciences Department, 1,
1470 [https://www.researchgate.net/publication/270577341_GRACE_AOD1B_product_description_document_for](https://www.researchgate.net/publication/270577341_GRACE_AOD1B_product_description_document_for_product_release_05_2014)
1471 [_product_release_05_2014](https://www.researchgate.net/publication/270577341_GRACE_AOD1B_product_description_document_for_product_release_05_2014).
- 1472 Frederikse, T., Riva, R. E., and King, M. A.: Ocean bottom deformation due to present-day mass redistribution
1473 and its impact on sea-level observations. *Geophys. Res. Lett.*, 44(24), 12–306,
1474 <https://doi.org/10.1002/2017GL075419>, 2017.
- 1475 Gardner, A. S., Moholdt, G., Cogley, J. G., Wouters, B., Arendt, A. A., Wahr, J., Berthier, E., Hock, R., Pfeffer,
1476 W. T., Kaser, G., Ligtenberg, S. R. M., Bolch, T., Sharp, M. J., Hagen, J. O., van den Broeke, M. R., and Paul,
1477 F.: A reconciled estimate of glacier contributions to sea level rise: 2003 to 2009, *Science*, 340(6134), 852–857,
1478 <https://doi.org/10.1126/science.1234532>, 2013.
- 1479 Gelaro, R., McCarty, W., Suárez, M. J., Todling, R., Molod, A., Takacs, L., Randles, C. A., Darmenov, A.,
1480 Bosilovich, M. G., Reichle, R., Wargan, K., Coy, L., Cullather, R., Draper, C., Akella, S., Buchard, V., Conaty,
1481 A., da Silva, A. M., Gu, W., Kim, G.-K., Koster, R., Lucchesi, R., Merkova, D., Nielsen, J. E., Partyka, G.,
1482 Pawson, S., Putman, W., Rienecker, M., Schubert, S. D., Sienkiewicz, M., and Zhao, B.: The modern-era
1483 retrospective analysis for research and applications, version 2 (MERRA-2), *J. Climate*, 30(14), 5419–5454,
1484 <https://doi.org/10.1175/JCLI-D-16-0758.1>, 2017.
- 1485 Good, S. A., M. J. Martin, and N. A. Rayner: EN4: Quality controlled ocean temperature and salinity profiles and
1486 monthly objective analyses with uncertainty estimates, *J. Geophys. Res. Oceans*, 118, 6704–6716,
1487 doi:10.1002/2013JC009067, 2013.
- 1488 Gregory, J. M., Griffies, S. M., Hughes, C. W., Lowe, J. A., Church, J. A., Fukimori, I., Gomez, N., Kopp, R. E.,
1489 Landerer, F., Le Cozannet, G., Ponte, R. M., Stammer, D., Tamisiea, M. E., and van de Wal, R. S. W.: Concepts
1490 and terminology for sea-level: mean, variability and change, both local and global, *Surv. Geophys.*, 40(6),
1491 1251–1289, <https://doi.org/10.1007/s10712-019-09525-z>, 2019
- 1492 Groh, A., Horwath, M., Horvath, A., Meister, R., Sørensen, L. S., Barletta, V. R., Forsberg, R., Wouters, B.,
1493 Ditmar, P., Ran, J., Klees, R., Su, X., Shang, K., Guo, J., Shum, C. C., Schrama, E., and Shepherd, A.:
1494 Evaluating GRACE Mass Change Time Series for the Antarctic and Greenland Ice Sheet—Methods and
1495 Results, *Geosci.*, 9(10), 415, <https://doi.org/10.3390/geosciences9100415>, 2019a.
- 1496 Groh, A., Horwath, M., Gutknecht, B. D., Hogg, A., Shepherd, A.: Improved estimates of Antarctic mass balance
1497 from updated GRACE solution series, Poster presented at ESA Living Planet Symposium 2019, Milano, 2019b.
- 1498 Gutknecht, B. D., Groh, A., Cáceres, D., and Horwath, M.: Assessing Global Ocean and Continental Mass Change
1499 from 17 years of GRACE/-FO: the role of coastal buffer zones, EGU General Assembly 2020, Online, 4–8
1500 May 2020, EGU2020-18038, <https://doi.org/10.5194/egusphere-egu2020-18038>, 2020.
- 1501 Haagmans, R., Siemes, C., Massotti, L., Carraz, O., and Silvestrin, P.: ESA’s next-generation gravity mission
1502 concepts. *Rendiconti Lincei. Scienze Fisiche e Naturali*, 1–11. <https://doi.org/10.1007/s12210-020-00875-0>,
1503 2020.



- 1504 Hanasaki, N., Kanae, S., Oki, T.: A reservoir operation scheme for global river routing models. *J. Hydrol.* 327 (1-
1505 2), 22–41. <https://doi.org/10.1016/j.jhydrol.2005.11.011>, 2006.
- 1506 Hamlington, B. D., Gardner, A. S., Ivins, E., Lenaerts, J. T., Reager, J. T., Trossman, D. S., Zaron, E. D., Adhikari,
1507 S., Arendt, A., Aschwanden, A., Beckley, B. D., Bekaert, D. P. S., Blewitt, G., Caron, L., Chambers, D. P.,
1508 Chandanpurkar, H. A., Christianson, K., Csatho, B., Cullather, R. I., DeConto, R. M., Fasullo, J. T., Frederikse,
1509 T., Freymueller, J. T., Gilford, D. M., Giroto, M., Hammond, W. C., Hock, R., Holschuh, N., Kopp, R. E.,
1510 Landerer, F., Larour, E., Menemenlis, D., Merrifield, M., Mitrovica, J. X., Nerem, R. S., Nias, I. J., Nieves,
1511 V., Nowicki, S., Pangaluru, K., Piecuch, C. G., Ray, R. D., Rounce, D. R., Schlegel, N.-J., Seroussi, H.,
1512 Shirzaei, M., Sweet, W. V., Velicogna, I., Vinogradova, N., Wahl, T., Wiese, D. N., Willis, M. J.:
1513 Understanding of Contemporary Regional Sea-Level Change and the Implications for the Future, *Rev.*
1514 *Geophys.*, 58(3), e2019RG000672, <https://doi.org/10.1029/2019RG000672>, 2020.
- 1515 Harris, I., Jones, P. D., Osborn, T. J., Lister, D. H.: Updated high-resolution grids of monthly climatic observations
1516 - the CRU TS3.10 Dataset, *Int. J. Climatol.* 34 (3), 623–642. <https://doi.org/10.1002/joc.3711>, 2014.
- 1517 Hartmann, D. L., Klein Tank, A.M.G., Rusticucci, M., Alexander, L. V., Brönnimann, S., Charabi, Y., Dentener,
1518 F. J., Dlugokencky, E. J., Easterling, D. R., Kaplan, A., Soden, B. J., Thorne, P. W., Wild, M., and Zhai, P. M.:
1519 Observations: Atmosphere and Surface. In: *Climate Change 2013: The Physical Science Basis. Contribution*
1520 *of Working Group I to the Fifth Assessment Report of the Intergovernmental Panel on Climate Change*
1521 *[Stocker, T.F., Qin, D., Plattner, G.-K., Tignor, M., Allen, S. K., Boschung, J., Nauels, A., Xia, Y., Bex, V.,*
1522 *and Midgley, P. M. (eds.)]. Cambridge University, <https://doi.org/10.1017/CBO9781107415324.008>, 2013.*
- 1523 Horwath, M., and Groh, A.: The GRACE mass change estimators developed for ESA’s CCI ice sheet mass balance
1524 products, *Proc. GRACE Science Team Meeting 2016*, Potsdam, 5-7 November 2016, [https://www.gfz-
1525 potsdam.de/en/section/global-geomonitoring-and-gravity-field/projects/gravity-recovery-and-climate-
1526 experiment-follow-on-grace-fo-mission/gstm/gstm-2016/](https://www.gfz-potsdam.de/en/section/global-geomonitoring-and-gravity-field/projects/gravity-recovery-and-climate-experiment-follow-on-grace-fo-mission/gstm/gstm-2016/), 2016.
- 1527 Horwath, M., Novotny, K., Cazenave, A., Palanisamy, H., Marzeion, B., Paul, F., Döll, P., Cáceres, D., Hogg, A.,
1528 Shepherd, A., Otsaka, I., Forsberg, R., Barletta, V. R., Simonsen, S., Andersen, O. B., Rose, S. K., Rannald,
1529 H., Johannessen, J. A., Raj, R. P., Gutknecht, B. D., Merchant, Ch. J., von Schuckmann, K.: ESA Climate
1530 Change Initiative (CCI) Sea-level Budget Closure (SLBC_cci). Product Description Document D2.4.2:
1531 Version 2 data sets and uncertainty assessments. Version 1.2, 18 Jun. 2019, 2019.
- 1532 Horwath, M., Gutknecht, B. D., Cazenave, A., Palanisamy, H. K., Marti, F., Marzeion, B., Paul, F., Le Bris, R.,
1533 Hogg, A. E., Otsaka, I., Shepherd, A., Döll, P., Cáceres, D., Müller Schmied, H., Johannessen, J. A., Nilsen,
1534 J. E. Ø., Raj, R. P., Forsberg, R., Sandberg Sørensen, L., Barletta, V. R., Simonsen, S., Knudsen, P., Andersen,
1535 O. B., Randall, H., Rose, S. K., Merchant, C. J., Macintosh, C. R., von Schuckmann, K., Novotny, K., Groh,
1536 A., Restano, M., Benveniste, J. (2021): ESA Sea Level Budget Closure Climate Change Initiative (SLBC_cci):
1537 Time series of global mean sea level budget and ocean mass budget elements (1993-2016, at monthly
1538 resolution), version 2.1, NERC EDS Centre for Environmental Data Analysis, 16 April 2021,
1539 <http://dx.doi.org/10.5285/1562578dd07844f19f01f0db9366106d>, 2021
- 1540 IPCC: IPCC Special Report on the Ocean and Cryosphere in a Changing Climate [Pörtner, H.-O., Roberts, D. C.,
1541 Masson-Delmotte, V., Zhai, P., Tignor, M., Poloczanska, E., Mintenbeck, K., Alegría, A., Nicolai, M., Okem,
1542 A., Petzold, J., Rama, B., Weyer, N. M. (eds.)], available at <https://www.ipcc.ch/srocc/>, 2019.
- 1543 Ishii, M. and Kimoto, M.: Reevaluation of Historical Ocean Heat Content Variations with Time-varying XBT and
1544 MBT Depth Bias Corrections, *J. Oceanogr.*, 65, 287–299, <https://doi.org/10.1007/s10872-009-0027-7>, 2009
- 1545 Ivins, E. R., James, T. S., Wahr, J., O. Schrama, E. J., Landerer, F. W., and Simon, K. M.: Antarctic contribution
1546 to sea-level rise observed by GRACE with improved GIA correction, *J. Geophys. Res.: Solid Earth*, 118(6),
1547 3126–3141, <https://doi.org/10.1002/jgrb.50208>, 2013.
- 1548 JCGM: Evaluation of measurement data—Guide to the expression of uncertainty in measurement, *Int. Organ.*
1549 *Stand. Geneva*, available under [https://www.bipm.org/utls/common/documents/jcgm/
1550 E.pdf](https://www.bipm.org/utls/common/documents/jcgm/JCGM_100_2008_-E.pdf), 2008
- 1551 Johnson, G. C. and Chambers, D. P.: Ocean bottom pressure seasonal cycles and decadal trends from GRACE
1552 Release-05: Ocean circulation implications, *J. Geophys. Res. Oceans*, 118, 4228–4240,
1553 <https://doi.org/10.1002/jgrc.20307>, 2013.
- 1554 Klinger, B., Mayer-Gürr, T., Behzadpour, S., Ellmer, M., Kvas, A., and Zehentner, N.: The new ITSG-Grace2016
1555 release, *Geophys. Res. Abstr.*, 18, EGU2016–11547, <https://doi.org/10.13140/RG.2.1.1856.7280>, 2016.
- 1556 Kobayashi, S., Ota, Y., Harada, Y., Ebata, A., Moriya, M., Onoda, H., Onogi, K., Kamahori, H., Kobayashi, C.,
1557 Endo, H., Miyaoka, K., and Takahashi, K.: The JRA-55 reanalysis: General specifications and basic
1558 characteristics, *J. Meteor. Soc. Japan. Ser. II*, 93(1), 5–48, <https://doi.org/10.2151/jmsj.2015-001>, 2015.
- 1559 Kusche, J., Schmidt, R., Petrovic, S., and Rietbroek, R.: Decorrelated GRACE time-variable gravity solutions by
1560 GFZ, and their validation using a hydrological model, *J. Geod.*, 83(10), 903–913,
1561 <http://dx.doi.org/10.1007/s00190-009-0308-3>, 2009.



- 1562 Kusche, J., Uebbing, B., Rietbroek, R., Shum, C. K., and Khan, Z. H.: Sea-level budget in the Bay of Bengal
1563 (2002–2014) from GRACE and altimetry, *J. Geophys. Res.: Oceans*, 121, 1194–1217,
1564 <https://doi.org/10.1002/2015JC011471>, 2016.
- 1565 Legeais, J. F., Ablain, M., Zawadzki, L., Zuo, H., Johannessen, J. A., Scharffenberg, M. G., Fenoglio-Marc, L.,
1566 Fernandes, J., Andersen, O. B., Rudenko, S., Cipollini, P., Quartly, G. D., Passaro, M., Cazenave, A., and
1567 Benveniste J.: An improved and homogeneous altimeter sea-level record from the ESA Climate Change
1568 Initiative, *Earth Syst. Sci. Data*, 10, 281–301, <https://doi.org/10.5194/essd-10-281-2018>, 2018.
- 1569 Lehner, B., Liermann, C. R., Revenga, C., Vörösmarty, C., Fekete, B., Crouzet, P., Döll, P., Endejan, M., Frenken,
1570 K., Magome, J., Nilsson, C., Robertson, J. C., Rödel, R., Sindorf, N., Wisser, D.: High-resolution mapping of
1571 the world's reservoirs and dams for sustainable river-flow management, *Front. Ecol. Environ.*, 9(9), 494–502,
1572 <https://doi.org/10.1890/100125>, 2011.
- 1573 Levitus S., Antonov, J. I., Boyer, T. P., Baranova, O. K., Garcia, H. E., Locarnini, R. A., Mishonov, A. V., Reagan,
1574 J. R., Seidov, D., Yarosh, E. S., Zweng, M. M.: World ocean heat content and thermocline sea-level change
1575 (0–2000 m), 1955–2010, *Geophys. Res. Lett.*, 39, L10603, <https://doi.org/10.1029/2012GL051106>, 2012.
- 1576 Ligtenberg, S. R. M., Helsen, M. M., and van den Broeke, M. R.: An improved semi-empirical model for the
1577 densification of Antarctic firn, *The Cryosphere*, 5, 809, <https://doi.org/10.5194/tcd-5-1921-2011>, 2011.
- 1578 Loomis, B. D., and Luthcke, S. B.: Mass evolution of Mediterranean, Black, Red, and Caspian Seas from GRACE
1579 and altimetry: accuracy assessment and solution calibration, *J. Geod.*, 91(2): 195–206,
1580 <https://doi.org/10.1007/s00190-016-0952-3>, 2017
- 1581 Loomis, B. D., Rachlin, K. E., and Luthcke, S. B.: Improved Earth oblateness rate reveals increased ice sheet
1582 losses and mass-driven sea-level rise, *Geophys. Res. Lett.*, 46(12), 6910–6917,
1583 <https://doi.org/10.1029/2019GL082929>, 2019.
- 1584 Luthcke, S. B., Sabaka, T. J., Loomis, B. D., Arendt, A. A., McCarthy, J. J., and Camp, J.: Antarctica, Greenland
1585 and Gulf of Alaska land-ice evolution from an iterated GRACE global mascon solution, *J. Glac.*, 59(216), 613–
1586 631. <https://doi.org/10.3189/2013JoG12J147>, 2013.
- 1587 Marzeion, B., Jarosch, A. H., and Hofer, M.: Past and future sealevel change from the surface mass balance of
1588 glaciers, *The Cryosphere*, 6, 1295–1322, <https://doi.org/10.5194/tc-6-1295-2012>, 2012.
- 1589 Maurer, J. M., Schaefer, J. M., Rupper, S., Corley, A.: Acceleration of ice loss across the Himalayas over the past
1590 40 years, *Sci. Adv.* 5(6), eaav7266, <https://doi.org/10.1126/sciadv.aav7266>, 2019.
- 1591 Mayer-Gürr, T., Behzadpour, S., Ellmer, M., Kvas, A., Klinger, B., and Zehentner, N.: ITSG-Grace2016 - Monthly
1592 and Daily Gravity Field Solutions from GRACE, GFZ Data Services, <https://doi.org/10.5880/icgem.2016.007>,
1593 2016.
- 1594 Mayer-Gürr, T., Behzadpour, S., Ellmer, M., Klinger, B., Kvas, A., Strasser, S., and Zehentner, N.:
1595 ITSG-Grace2018: The new GRACE time series from TU Graz, Abstract from GRACE / GRACE-FO
1596 Science Team Meeting 2018, Potsdam, Germany, 2018a.
- 1597 Mayer-Gürr, T., Behzadpur, S., Ellmer, M., Kvas, A., Klinger, B., Strasser, S., Zehentner, N.: ITSG-Grace2018 -
1598 Monthly, Daily and Static Gravity Field Solutions from GRACE, GFZ Data Services.
1599 <http://doi.org/10.5880/ICGEM.2018.003>, 2018b.
- 1600 McMillan, M., Leeson, A., Shepherd, A., Briggs, K., Armitage, T. W. K., Hogg, A., Kuipers Munneke, P., van
1601 den Broeke, M., Noël, B., van de Berg, W. J., Ligtenberg, S., Horwath, M., Groh, A., Muir, A. and Gilbert, L.:
1602 A high-resolution record of Greenland mass balance: High-Resolution Greenland Mass Balance, *Geophys.*
1603 *Res. Lett.*, 43, 7002–7010, <https://doi.org/10.1002/2016GL069666>, 2016.
- 1604 Merchant, C. J., Paul, F., Popp, T., Ablain, M., Bontemps, S., Defourny, P., Hollmann, R., Lavernge, T., Laeng,
1605 A., de Leeuw, G., Mittaz, J., Poulsen, C., Povey, A. C., Reuter, M., Sathyendranath, S., Sandven, S., Sofieva,
1606 V. F., and Wagner, W.: Uncertainty information in climate data records from Earth observation, *Earth Syst.*
1607 *Sci. Data*, 9(2), 511–527, <https://doi.org/10.5194/essd-9-511-2017>, 2017.
- 1608 Merchant, C. J., Embury, O., Bulgin, C. E., Block, T., Corlett, G. K., Fiedler, E., Good, S. A., Mittaz, J., Rayner,
1609 N. A., Berry, D., Eastwood, S., Taylor, M., Tsuchima, Y., Waterfall, A., Wilson, R. and Donlon, C.: Satellite-
1610 based time-series of sea-surface temperature since 1981 for climate applications, *Sci. Data*, 6, 223. ISSN 2052-
1611 4463, <https://doi.org/10.1038/s41597-019-0236-x>, 2019.
- 1612 Mottram, R., Simonsen, S. B., Høyer Svendsen, S., Barletta, V. R., Sandberg Sørensen, L., Nagler, T., Wuite, J.,
1613 Groh, A., Horwath, M., Rosier, J., Solgaard, A., Hvidberg, C. S., and Forsberg, R.: An integrated view of
1614 Greenland ice sheet mass changes based on models and satellite observations, *Remote Sensing*, 11(12), 1407,
1615 <https://doi.org/10.3390/rs11121407>, 2019.
- 1616 Müller Schmied, H., Eisner, S., Franz, D., Wattenbach, M., Portmann, F. T., Flörke, M., and Döll, P.: Sensitivity
1617 of simulated global-scale freshwater fluxes and storages to input data, hydrological model structure, human
1618 water use and calibration, *Hydrol. Earth Syst. Sci.* 18 (9), 3511–3538. <https://doi.org/10.5194/hess-18-3511-2014>, 2014.
- 1620 Müller Schmied, H., Cáceres, D., Eisner, S., Flörke, M., Herbert, C., Niemann, C., Peiris, T. A., Popat, E.,
1621 Portmann, F. T., Reinecke, R., Schumacher, M., Shadkam, S., Telteu, C.-E., Trautmann, T., and Döll, P.: The



- 1622 global water resources and use model WaterGAP v2.2d: model description and evaluation, *Geosci. Model*
1623 *Dev.*, 14, 1037–1079, <https://doi.org/10.5194/gmd-14-1037-2021>, 2021.
- 1624 Nagler, T., Floricioiu, D., Groh, A., Horwath, M., Kusk, A., Muir, A., and Wuite, J.: Algorithm Theoretical Basis
1625 Document (ATBD) for the Antarctic_Ice_Sheet_cci project of ESA's Climate Change Initiative, version 2.1,
1626 05 July 2018, available from: <http://www.esa-icesheets-antarctica-cci.org/>, 2018a.
- 1627 Nagler, T., et al.: Comprehensive Error Characterisation Report (CECR). Antarctic_Ice_Sheet_cci project, ESA's
1628 Climate Change Initiative, version 2.1, 05 July 2018, available from: <http://www.esa-icesheets-antarctica-cci.org/>, 2018b.
- 1629
- 1630 Nerem, R. S., Beckley, B. D., Fasullo, J. T., Hamlington, B. D., Masters, D., and Mitchum, G. T.: Climate-change–
1631 driven accelerated sea-level rise detected in the altimeter era, *P. Natl. Acad. Sci.*, 115 (9) 2022–2025,
1632 <https://doi.org/10.1073/pnas.1717312115>, 2018.
- 1633 New, M., Lister, D., Hulme, M., and Makin, I.: A high-resolution data set of surface climate over global land areas,
1634 *Clim. Res.*, 21(1), 1–25, <https://doi.org/10.3354/cr021001>, 2002.
- 1635 Nilsson, J., Vallelonga, P., Simonsen, S.B., Sørensen, L.S., Forsberg, R., Dahl-Jensen, D., Hirabayashi, M.:
1636 Greenland 2012 Melt Event Effects on CryoSat-2 Radar Altimetry, *Geophys. Res. Lett.* 42(10), 3919–26,
1637 doi:10.1002/2015GL063296, 2015.
- 1638 Oppenheimer, M., Glavovic, B.C., Hinkel, J., van de Wal, R., Magnan, A. K., Abd-Elgawad, A., Cai, R., Cifuentes-
1639 Jara, M., DeConto, R. M., Ghosh, T., Hay, T., Isla, R., Marzeion, B., Meyssignac, B., and Sebesvari, Z.: Sea-
1640 level Rise and Implications for Low-Lying Islands, Coasts and Communities. In: IPCC Special Report on the
1641 Ocean and Cryosphere in a Changing Climate [Pörtner, H.-O., Roberts, D. C., Masson-Delmotte, V., Zhai, P.,
1642 Tignor, M., Poloczanska, E., Mintenbeck, K., Alegria, A., Nicolai, M., Okem, A., Petzold, J., Rama, B., Weyer,
1643 N. M. (eds.)], available at <https://www.ipcc.ch/srocc/>, 2019.
- 1644 Peltier W. R.: Global glacial isostasy and the surface of the ice-age Earth: the ICE-5G (VM2) model and GRACE,
1645 *Annu. Rev. Earth Pl. Sc.*, 32:111, <https://doi.org/10.1146/annurev.earth.32.082503.144359>, 2004.
- 1646 Peltier, W. R., Argus, D. F., and Drummond, R.: Space geodesy constrains ice age terminal deglaciation: The
1647 global ICE-6G_C (VM5a) model: Global Glacial Isostatic Adjustment, *J. Geophys. Res. Solid Earth*, 120(1),
1648 450–487. <https://doi.org/10.1002/2014JB011176>, 2015.
- 1649 Pfeffer, W. T., Arendt, A. A., Bliss, A., Bolch, T., Cogley, J. G., Gardner, A. S., Hagen, J.-O., Hock, R., Kaser, G.,
1650 Kienholz, C., Miles, E. S., Moholdt, G., Mölg, N., Paul, F., Radic, V., Rastner, P., Raup, B. H., Rich, J., Sharp,
1651 M. J., and The Randolph Consortium: The Randolph Glacier Inventory: a globally complete inventory of
1652 glaciers, *J. Glac.*, 60(221), 537–552, <https://doi.org/10.3189/2014JoG13J176>, 2014.
- 1653 Poli, P., Hersbach, H., Dee, D. P., Berrisford, P., Simmons, A. J., Vitart, F., Laloyaux, P., Tan, D. G. H., Peubey,
1654 C., Thépaut, J.-N., Trémolet, Y., Hólm, E. V., Bonavita, M., Isaksen, L., and Fisher, M.: ERA-20C: An
1655 atmospheric reanalysis of the twentieth century, *J. Climate*, 29(11), 4083–4097, [https://doi.org/10.1175/JCLI-](https://doi.org/10.1175/JCLI-D-15-0556.1)
1656 [D-15-0556.1](https://doi.org/10.1175/JCLI-D-15-0556.1), 2016.
- 1657 Purkey, S. and Johnson, G. C.: Warming of global abyssal and deep Southern Ocean waters between the 1990s
1658 and 2000s: Contributions to global heat and sea-level rise budget, *J. Climate*, 23, 6336–6351,
1659 <https://doi.org/10.1175/2010JCLI3682.1>, 2010.
- 1660 Quartly, G. D., Legeais, J.-F., Ablain, M., Zawadzki, L., Fernandes, M. J., Rudenko, S., Carrère, L., García, P. N.,
1661 Cipollini, P., Andersen, O. B., Poisson, J.-C., Njiche, S.M., Cazenave A., and Benveniste J.: A new phase in
1662 the production of quality-controlled sea-level data, *Earth Syst. Sci. Data*, 9, 557–572,
1663 <https://doi.org/10.5194/essd-9-557-2017>, 2017.
- 1664 Quinn, K. J. and Ponte, R. M.: Uncertainty in ocean mass trends from GRACE, *Geophys. J. Int.*, 181, 762–768
1665 <https://doi.org/10.1111/j.1365-246X.2010.04508.x>, 2010.
- 1666 Raj, R. P., Andersen, O. B., Johannessen, J. A., Gutknecht, B. D., Chatterjee, S., Rose, S. K., Bonaduce, A.,
1667 Horwath, M., Rannal, H., Richter, K., Palanisamy, H., Ludwigsen, C. A., Bertino, L., Nilsen, J. E. Ø.,
1668 Knudsen, P., Hogg, A., Cazenave, A., Benveniste, J.: Arctic Sea Level Budget Assessment during the
1669 GRACE/Argo Time Period, *Remote Sens.* 2020, 12, 2837, <https://doi.org/10.3390/rs12172837>, 2020.
- 1670 Reager J. T., Gardner A. S., Famiglietti J. S., Wiese D. N., Eicker, A., and Lo M. H.: A decade of sea-level rise
1671 slowed by climate-driven hydrology, *Science*, 351(6274), 699–703. <https://doi.org/10.1126/science.aad8386>,
1672 2016.
- 1673 Rietbroek, R., Brunnabend, S.-E., Kusche, J., Schröter, J., and Dahle, C.: Revisiting the contemporary sea-level
1674 budget on global and regional scales, *P. Natl. Acad. Sci.* 2016 113 (6) 1504–1509,
1675 <https://doi.org/10.1073/pnas.1519132113>, 2016.
- 1676 Roemmich, D., Alford, M. H., Claustre, H., Johnson, K., King, B., Moum, J., Oke, P., Owens, W. B., Pouliquen,
1677 S., Purkey, S., Scanderbeg, M., Suga, T., Wijffels, S., Zilberman, N., Bakker, D., Baringer, M., Belbeoch, M.,
1678 Bittig, H. C., Boss, E., Calil, P., Carse, F., Carval, T., Chai, F., Conchubhair, D. Ó., d'Ortenzio, F., Dall'Olmo,
1679 G., Desbruyeres, D., Fennel, K., Fer, I., Ferrari, R., Forget, G., Freeland, H., Fujiki, T., Gehlen, M., Greenan,
1680 B., Hallberg, R., Hibiye, T., Hosoda, S., Jayne, S., Jochum, M., Johnson, G. C., Kang, K. R., Kolodziejczyk,
1681 N., Körzinger, A., Le Traon, P.-Y., Lenn, Y.-D., Maze, G., Mork, K. A., Morris, T., Nagai, T., Nash, J., Naveira



- 1682 Garbato, A., Olsen, A., Pattabhi, R. R., Prakash, S., Riser, S., Schmechtig, C., Schmid, C., Shroyer, E., Sterl,
1683 A., Sutton, P., Talley, L., Tanhua, T., Thierry, V., Thomalla, S., Toole, J., Troisi, A., Trull, T. W., Turton, J.,
1684 Velez-Belchi, P. J., Walczowski, W., Wang, H., Wanninkhof, R., Waterhouse, A. F., Waterman, S., Watson,
1685 A., Wilson, C. Wong, A. P. S., Xu, J. and Yasuda, I.: On the future of Argo: a global, full-depth, multi-
1686 disciplinary array. *Front. Mar. Sci.* 6:439. <https://doi.org/10.3389/fmars.2019.00439>, 2019.
- 1687 Royston, S., Vishwakarma, B. D., Westaway, R. M., Rougier, J., Sha, Z., and Bamber, J. L.: Can we resolve the
1688 basin-scale sea level trend budget from GRACE ocean mass? *J. Geophys. Res.: Oceans*, 125, e2019JC015535.
1689 <https://doi.org/10.1029/2019JC015535>, 2020.
- 1690 Saha, S., Moorthi, S., Pan, H. L., Wu, X., Wang, J., Nadiga, S., Tripp, P., Kistler, R., Woollen, J., Behringer, D.,
1691 Liu, H., Stokes, D., Grumbine, R., Gayno, G., Wang, J., Hour, Y.-T., Chuang, H.-Y., Juang, H.-M. H., Sela,
1692 J., Iredell, M., Treadon, R., Kleist, D., van Delst, P., Keyser, D., Derber, J., Ek, M., Meng, J., Wei, H., Yang,
1693 R., Lord, S., van den Dool, H., Kumar, A., Wang, W., Long, C., Chelliah, M., Xue, Y., Huang, B., Schemm,
1694 J., K., Ebisuzaki, W., Lin, R., Xie, P., Chen, M., Zhou, S., Higgins, W., Zou, C.-Z., Liu, Q., Chen, Y., Han, Y.,
1695 Cucurull, L., Reynolds, R. W., Rutledge, G., and Goldberg, M.: The NCEP climate forecast system reanalysis,
1696 *B. Am. Meteorol. Soc.*, 91(8), 1015-1058, <https://doi.org/10.1175/2010BAMS3001.1>, 2010.
- 1697 Scanlon, B. R., Zhang, Z., Save, H., Sun, A. Y., Schmied, H. M., van Beek, L. P., Wiese, D. N., Wada, Y., Long,
1698 D., Reedy, R. C., Longuevergne, L., Döll, P., and Bierkens, M. F. P.: Global models underestimate large
1699 decadal declining and rising water storage trends relative to GRACE satellite data, *P.Natl. Acad. Sci.*,
1700 201704665, 2018.
- 1701 Scharroo, R., Bonekamp, H., Ponsard, C., Parisot, F., von Engel, A., Tahtadjev, M., de Vriendt, K., and
1702 Montagner, F.: Jason continuity of services: continuing the Jason altimeter data records as Copernicus Sentinel-
1703 6, *Ocean Science*, 12(2), <https://doi.org/10.5194/os-12-471-2016>, 2016.
- 1704 Schneider, U., Becker, A., Finger, P., Meyer-Christoffer, A., Rudolf, B., Ziese, M.: GPCP Full Data Reanalysis
1705 Version 7.0 at 0.5°: Monthly Land-Surface Precipitation from Rain-Gauges built on GTS-based and Historic
1706 Data, Research Data Archive at the National Center for Atmospheric Research, Computational and Information
1707 Systems Laboratory, Boulder, Colo. (Updated irregularly.),
1708 https://doi.org/10.5676/DWD_GPCP/FD_M_V7_050, 2015.
- 1709 Shepherd, A., Ivins, E., Rignot, E., Smith, B., van den Broeke, M., Velicogna, I., Whitehouse, P., Briggs, K.,
1710 Joughin, I., Krinner, G., Nowicki, S., Payne, T., Scambos, T., Schlegel, N. A. G., Agosta, C., Ahlström, A.,
1711 Babonis, G., Varletta, V., Blazquez, A., Bonin, J., Csatho, B., Cullather, R., Felikson, D., Fettweis, X.,
1712 Forsberg, R., Gallee, H., Gardner, A., Gilbert, L., Groh, A., Gunter, B., Hanna, E., Harig, C., Helm, V.,
1713 Horvath, A., Horwath, M., Khan, S., Kjeldsen, K. K., Konrad, H., Langen, P., Lecavalier, B., Loomis, B.,
1714 Luthcke, S., McMillan, M., Melinie, D., Mernild, S., Mohajerani, Y., Moore, P., Mougnot, J., Moyano, G.,
1715 Muir, A., Nagler, T., Niell, G., Nilsson, J., Noel, B., Otsuka, I., Pattie, M. E., Peltier, W. R., Pie, N., Rietbroek,
1716 R., Rott, H., Sandberg-Sørensen, L., Sasgen, I., Save, H., Scheuchl, B., Schrama, E., Schröder, L., Seo, K.-W.,
1717 Simonsen, S., Slater, T., Spada, G., Sutterley, T., Talpe, M., Tarasov, Lev, van de Berg, W. J., van der Wal,
1718 W., van Wessel, M., Vishwakarma, B. D., Wiese, D., and Wouters, B.: Mass balance of the Antarctic Ice
1719 Sheet from 1992 to 2017, *Nature*, 556, 219-222, <https://doi.org/10.1038/s41586-018-0179-y>, 2018
- 1720 Shepherd, A., Gilbert, L., Muir, A. S., Konrad, H., McMillan, M., Slater, T., Briggs, K. H., Sundal, A. V., Hogg,
1721 A. E. & Engdahl, M.: Trends in Antarctic Ice Sheet Elevation and Mass, *Geophys. Res. Lett.*, 46(14), 8174-
1722 8183, <https://doi.org/10.1029/2019GL082182>, 2019.
- 1723 Simonsen, S. B., Barletta, V. R., Colgan, W. T., and Sørensen, L. S.: Greenland Ice Sheet Mass Balance (1992–
1724 2020) From Calibrated Radar Altimetry, *Geophys. Res. Lett.*, 48(3), e2020GL091216, 2021.
- 1725 Slater, T., Lawrence, I. R., Otsuka, I. N., Shepherd, A., Gourmelen, N., Jakob, L., Tepes, P., Gilbert, L., and
1726 Nienow, P.: Review Article: Earth's ice imbalance, *The Cryosphere*, 15, 233–246, <https://doi.org/10.5194/tc-15-233-2021>, 2021
- 1727 Sørensen, L.S., Simonsen, S. B., Nielsen, K., Lucas-Picher, P., Spada, G., Adalgeirsdottir, G., Forsberg, R., and
1728 Hvidberg, C.: Mass balance of the Greenland ice sheet (2003–2008) from ICESat data—the impact of
1729 interpolation, sampling and firn density, *The Cryosphere*, 5, 173-186, <https://doi.org/10.5194/tc-5-173-2011>,
1730 2011.
- 1731 Sørensen L.S., et al.: Product Specification Document (PSD) for the Greenland_Ice_Sheet_cci project of ESA's
1732 Climate Change Initiative, version 2.3 (ST-DTU-ESA-GISCCI-PSD-001), 20 March 2017, 2017.
- 1733 Sørensen, L. S., Simonsen, S. B., Forsberg, R., Khvorostovsky, K., Meister, R., and Engdahl, M. E.: 25 years of
1734 elevation changes of the Greenland Ice Sheet from ERS, Envisat, and CryoSat-2 radar altimetry, *Earth Planet.*
1735 *Sc. Lett.*, 495, 234-241, <https://doi.org/10.1016/j.epsl.2018.05.015>, 2018.
- 1736 Stammer, D., Cazenave, A., Ponte, R. M., and Tamisiea, M. E. : Causes for contemporary regional sea level
1737 changes, *Annu. Rev. Mar. Sci.*, 5, 21-46., <https://doi.org/10.1146/annurev-marine-121211-172406>, 2013
- 1738 Swenson, S., Chambers, D., and Wahr, J.: Estimating geocenter variations from a combination of GRACE and
1739 ocean model output, *J. Geophys. Res.: Solid Earth*, 113(B8), <https://doi.org/10.1029/2007JB005338>, 2008.
- 1740



- 1741 Tamisiea, M. E., and Mitrovica, J. X.: The moving boundaries of sea-level change: Understanding the origins of
1742 geographic variability, *Oceanography* 24(2):24–39, doi:10.5670/oceanog.2011.25, 2011.
- 1743 Tapley, B. D., Watkins, M. M., Flechtner, F., Reigber, C., Bettadpur, S., Rodell, M., Sasgen, I., Fmiglietti, J. S.,
1744 Landerer, F. W., Chambers, D. P., Reager, J. T., Gardner, A. S., Save, H., Ivins, E. R., Swenson, S. C., Boening,
1745 C., Dahle, C., Wiese, D. N., Dobslaw, H., Tamisiea, M. E., and Velicogna, I.: Contributions of GRACE to
1746 understanding climate change, *Nat. Clim. Change*, 9(5), 358–369, <https://doi.org/10.1038/s41558-019-0456-2>,
1747 2019.
- 1748 Trenberth, K. E.: Challenges for observing and modeling the global water cycle, *Remote Sens. Terr. Water Cycle*,
1749 32, 511–519, <https://doi.org/10.1002/9781118872086.ch32>, 2014.
- 1750 Uebbing, B., Kusche, J., Rietbroek, R., & Landerer, F. W.: Processing choices affect ocean mass estimates from
1751 GRACE, *J. Geophys. Res.: Oceans*, 124(2), 1029–1044, <https://doi.org/10.1029/2018JC014341>, 2019.
- 1752 Vishwakarma, B. D., Royston, S., Riva, R. E. M., Westaway, R. M., and Bamber, J. L.: Sea-level budgets should
1753 account for ocean bottom deformation, *Geophys. Res. Lett.*, 47(3), e2019GL086492,
1754 <https://doi.org/10.1029/2019GL086492>, 2020.
- 1755 von Schuckmann, K. and Le Traon, P.-Y.: How well can we derive Global Ocean Indicators from Argo data?,
1756 *Ocean Sci.*, 7(6), 783–791, <https://doi.org/10.5194/osd-8-999-2011>, 2011.
- 1757 von Schuckmann, K., Cheng, L., Palmer, M. D., Hansen, J., Tassone, C., Aich, V., Adusumilli, S., Beltrami, H.,
1758 Boyer, T., Cuesta-Valero, F. J., Desbruyères, D., Domingues, C., García-García, A., Gentile, P., Gilson, J.,
1759 Gorfer, M., Haimberger, L., Ishii, M., Johnson, G. C., Killick, R., King, B. A., Kirchengast, G., Kolodziejczyk,
1760 N., Lyman, J., Marzeion, B., Mayer, M., Monier, M., Monselesan, D. P., Purkey, S., Roemmich, D., Schweiger,
1761 A., Seneviratne, S. I., Shepherd, A., Slater, D. A., Steiner, A. K., Straneo, F., Timmermans, M.-L., and Wijffels,
1762 S. E.: Heat stored in the Earth system: where does the energy go?, *Earth Syst. Sci. Data*, 12, 2013–2041,
1763 <https://doi.org/10.5194/essd-12-2013-2020>, 2020.
- 1764 von Schuckmann, K., Palmer, M. D., Trenberth, K. E., Cazenave, A., Chambers, D., Champollion, N., Hansen, J.,
1765 Josey, A., Loeb, N., Mathieu, P. P., Meyssignac, B., Wild, M.: An imperative to monitor Earth’s energy
1766 imbalance, *Nat. Clim. Change* 6:138–144. doi:10.1038/nclimate2876, 2016
- 1767 Wada, Y., Reager, J. T., Chao, B. F., Wang, J., Lo, M.-H., Song, C., Li, Y., and Gardner, A. S.: Recent Changes
1768 in Land Water Storage and its Contribution to Sea-level Variations, *Surv. Geophys.*, 38(1), 131–152,
1769 <https://doi.org/10.1007/s10712-016-9399-6>, 2017.
- 1770 Wahr, J., Molenaar, M., and Bryan, F.: Time variability of the Earth’s gravity field: Hydrological and oceanic
1771 effects and their possible detection using GRACE, *J. Geophys. Res.*: 103(B12), 30205–30229,
1772 <https://doi.org/10.1029/98JB02844>, 1998.
- 1773 WCRP Global Sea-level Budget Group (the): Global sea-level budget, 1993-present, *Earth Syst. Sci. Data*, 10,
1774 1551–1590, <https://doi.org/10.5194/essd-10-1551-2018>, 2018.
- 1775 Weedon, G. P., Balsamo, G., Bellouin, N., Gomes, S., Best, M. J., and Viterbo, P.: The WFDEI meteorological
1776 forcing data set: WATCH Forcing Data methodology applied to ERA-Interim reanalysis data, *Water Resour.*
1777 *Res.* 50 (9), 7505–7514, <https://doi.org/10.1002/2014WR015638>, 2014.
- 1778 WGMS: Fluctuations of Glaciers Database, World Glacier Monitoring Service, Zurich, Switzerland,
1779 <https://doi.org/10.5904/wgms-fog-2018-11>. Online access: <http://dx.doi.org/10.5904/wgms-fog-2018-11>,
1780 2018
- 1781 Whitehouse P., Bentley M., Milne, G., King, M., and Thomas, I.: A new glacial isostatic adjustment model for
1782 Antarctica: calibrated and tested using observations of relative sea-level change and present-day uplift rates,
1783 *Geophys. J. Int.*, 190(3), 1464–1482, <https://doi.org/10.1111/j.1365-246X.2012.05557.x>, 2012.
- 1784 Zemp, M., Huss, M., Thibert, E., Eckert, N., McNabb, R., Huber, J., Barandun, M., Machguth, H., Nussbaumer,
1785 S. U., Gärtner-Roer, I., Thomson, L., Paul, F., Maussion, F., Kutuzov, S., Cogley, J. G.: Global glacier mass
1786 changes and their contributions to sea-level rise from 1961 to 2016, *Nature* 568, 382–386,
1787 <https://doi.org/10.1038/s41586-019-1071-0>, 2019.
- 1788 Zhou, Y., Li, Z., Li, J., Zhao, R., and Ding, X.: Glacier mass balance in the Qinghai–Tibet Plateau and its
1789 surroundings from the mid-1970s to 2000 based on Hexagon KH-9 and SRTM DEMs, *Rem. Sens. Environ.*,
1790 210, 96–112, <https://doi.org/10.1016/j.rse.2018.03.020>, 2018.
- 1796